

# 1 **Corticothalamic feedback sculpts visual spatial 2 integration in mouse thalamus**

3 **Gregory Born<sup>1,2,\*</sup>, Sinem Erisken<sup>1,3,4,\*</sup>, Felix A. Schneider<sup>1,2,\*</sup>, Agne Klein<sup>3</sup>, Milad H.  
4 Mobarhan<sup>5,6</sup>, Chu Lan Lao<sup>7,8</sup>, Martin A. Spacek<sup>1</sup>, Gaute T. Einevoll<sup>9,10</sup>, and Laura  
5 Busse<sup>1,11,+</sup>**

6 <sup>1</sup>Division of Neurobiology, Department Biology II, LMU Munich, 82151 Munich, Germany

7 <sup>2</sup>Graduate School of Systemic Neuroscience (GSN), LMU Munich, 82151 Munich, Germany

8 <sup>3</sup>Werner Reichardt Centre for Integrative Neuroscience, University of Tübingen, 72076 Tübingen, Germany

9 <sup>4</sup>Graduate School of Neural & Behavioural Sciences, International Max Planck Research School, University of  
10 Tübingen, 72074 Tübingen, Germany

11 <sup>5</sup>Centre for Integrative Neuroplasticity, University of Oslo, 0316 Oslo, Norway

12 <sup>6</sup>Department of Biosciences, University of Oslo, 0316 Oslo, Norway

13 <sup>7</sup>Department of Physiological Genomics, Biomedical Center (BMC), LMU Munich, 82152 Munich, Germany

14 <sup>8</sup>Institute of Stem Cell Research, Helmholtz Center Munich, Biomedical Center (BMC), 82152 Munich, Germany

15 <sup>9</sup>Faculty of Science and Technology, Norwegian University of Life Sciences, 1432 Aas, Norway

16 <sup>10</sup>Department of Physics, University of Oslo, 0371 Oslo, Norway

17 <sup>11</sup>Bernstein Centre for Computational Neuroscience, 82151 Munich, Germany

18 <sup>\*</sup>these authors contributed equally to this work

19 <sup>+</sup>busse@bio.lmu.de

## 20 **ABSTRACT**

En route from retina to cortex, visual information travels through the dorsolateral geniculate nucleus of the thalamus (dLGN), where extensive cortico-thalamic (CT) feedback has been suggested to modulate spatial processing. How this modulation arises from direct excitatory and indirect inhibitory CT feedback components remains enigmatic. We show that in awake mice topographically organized cortical feedback modulates spatial integration in dLGN by sharpening receptive fields (RFs) and increasing surround suppression. Guided by a network model revealing wide-scale inhibitory CT feedback necessary to reproduce these effects, we targeted the visual sector of the thalamic reticular nucleus (visTRN) for recordings. We found that visTRN neurons have large receptive fields, show little surround suppression, and have strong feedback-dependent responses to large stimuli, making them an ideal candidate for mediating feedback-enhanced surround suppression in dLGN. We conclude that cortical feedback sculpts spatial integration in dLGN, likely via recruitment of neurons in visTRN.

## 22 **Introduction**

Feedforward processing is a fundamental model of how the brain mediates vision. Using a largely feedforward architecture, artificial neural networks can now carry out robust and dynamic visual tasks that rival human performance, including visual object recognition<sup>1,2</sup>, inference of depth and 3D structure from 2D images<sup>3,4</sup> and semantic segmentation<sup>5,6</sup>. Inspired by the early visual system, these deep convolutional neural networks process visual information feedforward through a hierarchy of layers. These layers each contain small computational units that, similar to real neurons operating within their receptive field (RF), are applied to small patches of the image and during learning acquire selectivity for certain visual features. Remarkably, such feature maps found in artificial networks resemble those of real neurons<sup>7-9</sup>, and the activity of various layers along the artificial feedforward hierarchy can predict responses of real neurons in various cortical visual areas<sup>2,9-11</sup>. Besides providing a framework for machine vision, the feedforward architecture is also powerful for biological vision, where the initial feedforward sweep contains a significant amount of information, sometimes sufficient to drive perception<sup>12-14</sup>.

So why then, is feedback such a prominent and ubiquitous motif in the brain, where descending projections generally

34 tend to outnumber ascending afferents? For instance, most inputs to primary sensory cortical areas do not come from primary  
35 thalamus, but from higher-order structures<sup>15</sup>. The same principle applies to cortico-thalamic (CT) communication: relay cells  
36 in the dorsolateral geniculate nucleus (dLGN) of the thalamus receive only 5-10% of their synaptic inputs from retinal afferents,  
37 whereas 30% originate from L6 cortico-thalamic (L6CT) pyramidal cells of primary visual cortex (V1)<sup>16</sup>.

38 Similar to a lack of general consensus regarding the function of cortico-cortical feedback<sup>17,18</sup>, how CT feedback influences  
39 the representation of visual information remains poorly understood. Despite massive cortical input, dLGN RFs closely resemble  
40 retinal RFs rather than cortical ones<sup>19-22</sup>. Indeed, instead of driving dLGN RFs directly, CT feedback is considered a thalamic  
41 modulator, and implicated in more subtle changes of dLGN responses<sup>23</sup>. These changes are likely to be complex, given that  
42 both direct excitatory and indirect inhibitory CT feedback exert influences via local inhibitory interneurons in dLGN and  
43 inhibitory neurons in the thalamic reticular nucleus (TRN). The balance between these two feedback pathways might vary,  
44 given their differential stimulus selectivity and synaptic properties<sup>24,25</sup>.

45 Most notably, the retinotopic arrangement of CT projections known from primates and cats<sup>26-30</sup> is highly suggestive of a  
46 role in modulating spatial processing, yet experiments investigating spatial integration have yielded conflicting results: while  
47 some argue that surround suppression in dLGN relies entirely on intra-thalamic or retinal mechanisms<sup>31,32</sup>, there is evidence  
48 that CT feedback can sharpen spatial integration<sup>33-39</sup>. Recent optogenetic investigations in mice have failed to clarify the matter.  
49 Indeed, while Olsen et al.<sup>40</sup> report data consistent with a role of feedback in strengthening the inhibitory surround, other studies  
50 fail to observe any effect of CT feedback on spatial integration<sup>41</sup>, or even on any aspect of mouse dLGN activity<sup>42,43</sup>.

51 Here, we investigated the role of cortical feedback in modulating thalamic spatial integration across V1, dLGN, and visual  
52 TRN (visTRN), the main processing stages of the thalamo-cortico-thalamic loop. Using viral labeling and channelrhodopsin  
53 (ChR2)-assisted functional mapping, we found that V1 corticogeniculate feedback projections in the mouse have topographic  
54 organization and spatially specific functions. We used optogenetic manipulations to compare the modulation of dLGN responses  
55 by CT feedback to various stimulus sizes, and found that CT feedback enhanced effects of spatial context by sharpening RFs  
56 and increasing surround suppression. Computational modelling and recordings from the TRN suggest that CT feedback can  
57 augment dLGN surround suppression via visTRN. We conclude that CT feedback sculpts spatial integration in dLGN, likely  
58 via recruitment of inhibitory neurons in TRN.

## 59 Results

### 60 Anatomy of V1 corticogeniculate projections is consistent with topographic organization

61 To examine the anatomical spatial specificity of CT feedback in mouse dLGN, we expressed ChR2-eYFP in a localized  
62 population of L6CT pyramidal cells by injecting a small volume of cre-dependent AAV into V1 of Ntsr1-Cre mice<sup>44</sup> (**Figure 1a**),  
63 and registered the *post-mortem* histological data from individual mice into a 3D standardized anatomical coordinate system  
64 (Allen Mouse Common Coordinate Framework [CCF]<sup>45</sup>) (**Figure S1**). Visual inspection of brain slices revealed eYFP  
65 expression in somata and intracortical processes of L6CT cells within a restricted zone in V1 (**Figure 1b**); similarly, eYFP  
66 signals from axon terminals were also restricted to a localized zone in dLGN (**Figure 1c**). This shows that the population of  
67 transduced V1 L6CT neurons had a spatially specific innervation pattern in dLGN. Consistent with topographical mapping,  
68 these expression zones in V1 and dLGN seemed to cover overlapping regions of retinotopic space, in particular around the  
69 medial visual field, which is represented in the antero-lateral part of V1<sup>46,47</sup> and around the ipsilateral eye patch in dLGN<sup>48</sup>.  
70 This pattern is consistent with previous tracing studies in cats and primates, demonstrating a retinotopic organization of  
71 corticogeniculate feedback<sup>26-30</sup>.

72 How spatially condensed is this corticogeniculate projection zone? We next computed the relative volumes of transduced  
73 V1 CT pyramidal cells within L6 (“source volume”, **Figure 1d**) and their dLGN projections (“target volume”, **Figure 1e**). In  
74 this example mouse, transduced V1 CT neurons were located antero-laterally in V1, where they occupied 25% of L6; likewise,  
75 their thalamic projections were restricted to the medial edge of dLGN, where they covered a similar relative volume (15%,  
76 **Figure 1d,e**). We observed a corresponding pattern across mice (n = 3, **Figure S1**): dLGN target volumes were comparable to,  
77 or even smaller than, V1 source volumes (**Figure 1f**), which might be expected due to lateral arborizations of L6CT pyramidal  
78 cells contributing to our estimate of the V1 source volume. The general similarity of relative expression volumes is consistent  
79 with corticogeniculate feedback projections in mice having topography, and indicates that CT feedback could be well suited to  
80 provide local modulations of dLGN activity.

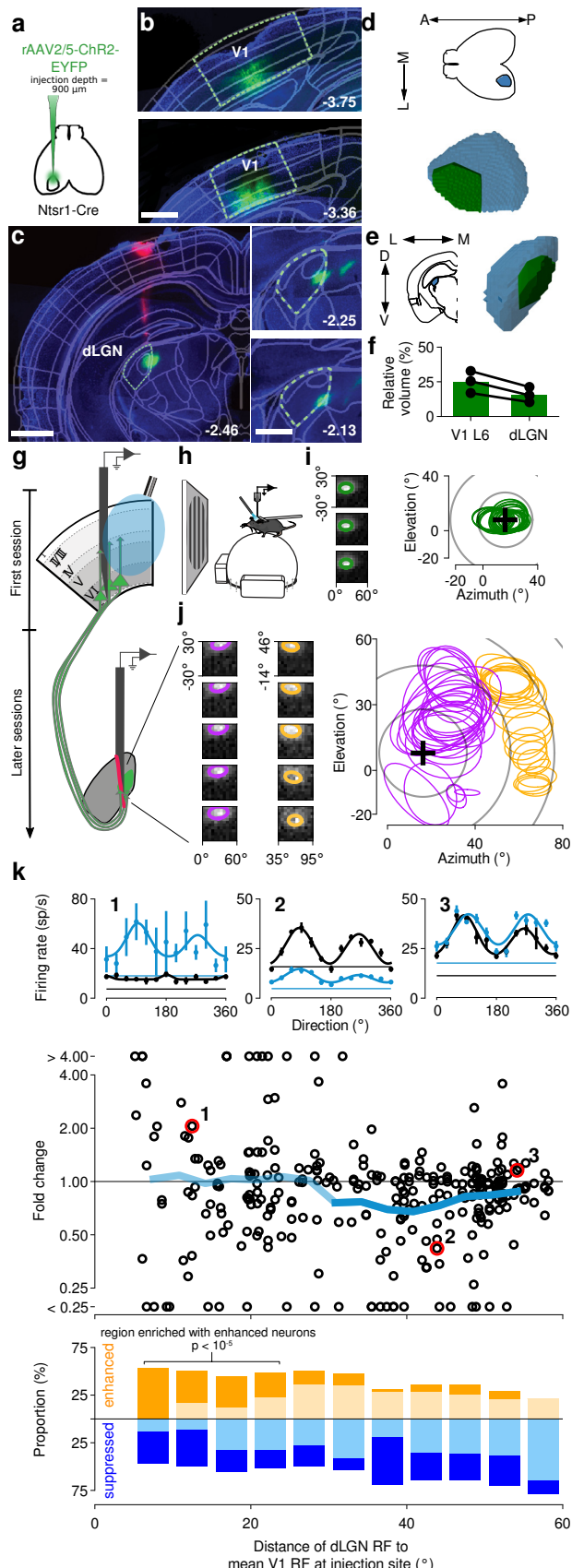


**Figure 1 (Previous page)** Anatomical and functional mapping of L6CT feedback.

**(a)** Schematic of viral transduction of a local population of V1 L6CT neurons with cre-dependent AAV-ChR2-eYFP in Ntsr1-cre mice<sup>44</sup>. **(b)** Coronal sections close to the V1 injection site for an example Ntsr1-Cre mouse, overlaid with fitted area boundaries from the Allen CCF<sup>45</sup> (gray). *Blue*: DAPI; *green*: eYFP; scale bar 0.5 mm. **(c)** Coronal sections of the transduced L6CT neurons' dLGN axonal projection. *Magenta*: DiI for reconstruction of recording track; *left*: scale bar 1 mm; *right*: scale bar 0.5 mm. **(b,c)** Numbers indicate distance from *bregma*. **(d)** *Top*: Axial schematic of V1 L6 (*blue*) within cortex (*black contour*). *Bottom*: 3D reconstruction of expression volume (*green*) within the V1 L6 volume (*blue*). Relative volume: 25%. Same perspective as in *Top*. **(e)** *Left*: Coronal schematic of dLGN (*blue*) within brain section (*black contour*). *Right*: 3D reconstruction of expression volume (*green*) within the dLGN volume (*blue*). Relative volume: 15%. Same perspective as in *Left*. **(f)** Relative expression volumes (expression volume/host area volume) for each mouse (*black dots*,  $n = 3$ ) and means across mice (*green bars*). **(g)** Schematic of ChR2-assisted, functional connectivity mapping. **(h)** Schematic of setup for *in vivo* recordings in head-fixed mice. **(i)** RF mapping in V1. *Left*: Spatial RFs for 3 example channels recorded at the V1 injection site. Colored circles represent  $1\sigma$  contours of fitted 2D Gaussian. *Right*: All fitted V1 RF contours from the example session. Black cross: mean RF center. **(j)** RF mapping in dLGN. *Left*: Spatial RFs and fitted  $1\sigma$  contours for example channels located in dLGN (two recording sessions, channel order top-to-bottom, as on probe). *Right*: Fitted dLGN RF contours with mean RF position from V1 recording indicated by black cross. **(k)** Spatial profile of modulations by photostimulation of CT feedback. *Top*: Direction tuning curves of 3 example neurons during photostimulation of L6CT pyramidal cells (*blue*) and control conditions (*black*). *Horizontal lines*: spontaneous firing rates. *Middle*: CT feedback modulation strength (fold change) as a function of retinotopic distance to the mean V1 RF position at the injection site. *Red*: example neurons, numbers correspond to numbers in *Top*; *blue line*: Mean of fold change values in overlapping bins (bin size 15 deg, spacing 3.3 deg), *thick portion*: region with significant mean fold change ( $n = 293$  neurons,  $p = 6.8 \times 10^{-3}$ , cluster permutation test). *Bottom*: Proportions of significantly enhanced (*dark orange*), suppressed (*dark blue*) and not modulated neurons (*pale*).

81 **ChR2-assisted functional mapping of CT feedback yields a mix of enhancement and suppression at near  
82 regions, and suppression at distance**

83 To examine whether the topographically organized corticogeniculate feedback can also generate spatially specific functional  
84 effects, we next probed the impact of CT feedback on dLGN responses using ChR2-assisted functional mapping (**Figure 1g**).  
85 Assuming that the observed topography of CT feedback projections is closely linked to retinotopy, we exploited RF position  
86 as a functional distance metric between the transduced L6CT population and the geniculate neurons in their target zone. In  
87 head-fixed mice (**Figure 1h**), we performed silicon probe recordings first at the V1 injection site and used a sparse noise stimulus  
88 to estimate average RF location (**Figure 1i**). We then turned to dLGN, where RF mapping revealed a smooth progression of  
89 retinotopy typical of mouse dLGN<sup>48</sup>, with RFs covering positions from upper to lower visual field for consecutive recording  
90 channels along the dorso-ventral axis (**Figure 1j**). Through multiple sessions with different insertions, we were able to measure  
91 dLGN RFs located at a wide range of distances from the averaged RF at the V1 injection site.

92 We next functionally mapped the spatial profile of CT feedback effects by photostimulating the local population of  
93 transduced L6CT pyramidal cells during the presentation of full-field drifting gratings (**Figure 1k**). To avoid potentially  
94 confounding effects of locomotion<sup>49,50</sup>, we only considered trials in which the animal was quiescent (speed  $\leq 0.25$  cm/s for  
95  $\geq 80\%$  of the trial) for computing direction tuning curves. From these curves (**Figure 1k**, top), we determined, for each neuron,  
96 the relative CT feedback modulation strength as the ratio of responses with L6CT photostimulation and in control conditions  
97 (fold change). Across the population of recorded dLGN neurons, activating CT feedback resulted in both enhanced ( $n = 112$ )  
98 and suppressed neurons ( $n = 181$ ), with diverse effect sizes.

99 Mapping CT feedback modulation of individual neurons against the retinotopic distance from the activated L6CT pyramidal  
100 cell population, however, revealed a distinct spatial profile (**Figure 1k**, middle): while CT feedback, on average, had a small  
101 effect in retinotopically “near” regions ( $< 30$  deg), average CT feedback modulation in “distant” regions was predominantly  
102 suppressive ( $30 - 53$  deg,  $p = 6.8 \times 10^{-3}$ , cluster permutation test; thick blue line). The small average effect in “near”  
103 regions, rather than showing no modulation at all, reflected the diversity of effects (**Figure 1k**, bottom). Indeed, when we  
104 classified neurons into significantly enhanced, suppressed or not modulated by CT feedback, we observed that the prevalence of  
105 modulation types depended on retinotopic distance ( $p = 7.2 \times 10^{-3}$ , Chi-square test). Unlike suppressed neurons which were  
106 stably distributed across retinotopic distance ( $p = 0.43$ , Chi-square test), enhanced neurons varied significantly with distance  
107 ( $p = 4.7 \times 10^{-4}$ , Chi-square test) and were significantly enriched from  $0 - 25$  deg ( $p < 10^{-5}$ , cluster permutation test).

108 Together with our anatomical data, these findings demonstrate that L6CT pyramidal cell output impacts mouse dLGN  
109 activity with a specific spatial profile. This profile is consistent with a circuit architecture, where enhancing influences of CT  
110 feedback are more localized, while suppressive influences have a wider spatial scale. This spatial profile, in particular the  
111 distant suppressive region, is suggestive of L6CT feedback being involved in shaping dLGN spatial integration and surround  
112 suppression.

### 113 **CT feedback modulates dLGN spatial integration by sharpening RFs and increasing surround suppression**

114 Having observed that photostimulation of CT feedback can, in principle, induce modulations of geniculate activity with a  
115 spatial profile suggestive of shaping dLGN spatial integration, we next set out to probe whether CT feedback is indeed involved  
116 in tuning for stimulus size and surround suppression (**Figure 2**). Surround suppression refers to the reduction of a neuron's  
117 activity in response to a stimulus exceeding its classical RF (**Figure 2d**), and is thought to be important for integrating local  
118 information within a more global context.

119 L6CT neurons are known for having low firing rates<sup>51</sup> and for controlling the gain of the entire cortical column<sup>40,52-54</sup>;  
120 hence, to avoid potential concerns that direct L6 photoactivation might induce aberrant response patterns, we instead suppressed  
121 activity of L6CT neurons. To this end, we employed a strategy of reliable and powerful global V1 suppression, by exploiting  
122 reversible optogenetic activation of the major class of V1 inhibitory interneurons, PV+ interneurons<sup>55,56</sup> (**Figure 2a**). We  
123 selectively targeted PV+ neurons to express ChR2 by injecting cre-dependent AAV into V1 of PV-Cre mice. Recording  
124 extracellular activity across the layers of V1, we verified that optogenetic activation of PV+ neurons suppressed output across  
125 the cortical column (**Figure 2b,c**). We found that, even in the presence of drifting gratings, which powerfully drive V1 activity in  
126 control conditions (**Figure 2b**), optogenetic activation of PV+ inhibitory interneurons led to significant suppression of responses  
127 in V1 neurons across supragranular (S, n = 52), granular (G, n = 50) and infragranular (I, n = 82) layers (all  $p < 5.1 \times 10^{-3}$ ,  
128 Wilcoxon signed-rank test; **Figure 2c**).

129 Having confirmed that photostimulation of PV+ interneurons suppressed V1 activity, including in infragranular layers,  
130 we next turned to the thalamus and recorded from the dLGN (**Figure 2e-l**). Because dLGN RF locations in single electrode  
131 penetrations vary widely across simultaneously recorded neurons (e.g., **Figure 1j**), measuring complete size tuning curves for  
132 dLGN neurons with RF-centered stimuli is laborious. We hence decided to first focus on conditions without a visual stimulus,  
133 corresponding to 0 deg conditions in size tuning experiments (**Figure 2d**). Given a previous study showing that mouse dLGN  
134 responses to full-field gratings during V1 suppression were enhanced<sup>40</sup>, we were surprised to observe that in response to a  
135 uniform gray screen (corresponding to a 0 deg size stimulus), suppressing visual cortex, for both shorter (250 ms; **Figure 2e1**)  
136 and longer (1 s; **Figure 2e2**) periods, resulted in reduced geniculate activity. Indeed, firing rates of dLGN neurons during the  
137 window of V1 suppression were lower than in the equally sized window before V1 suppression (during: 3.7 sp/s vs. before:  
138 4.9 sp/s; n = 276 neurons;  $p = 1.5 \times 10^{-5}$ , Wilcoxon signed-rank test; **Figure 2f**). Furthermore, a closer inspection of the  
139 spike rasters (**Figure 2e**) centered around V1 suppression revealed a change in dLGN spiking patterns: the ratio of spikes  
140 fired in bursts (red) approximately doubled (during: 12.7% vs. before: 5.1%; n = 232 neurons;  $p = 4.1 \times 10^{-11}$ , Wilcoxon  
141 signed-rank test; **Figure 2g**). Furthermore, V1 suppression shifted the entire distribution of burst lengths towards higher  
142 numbers ( $p = 3.6 \times 10^{-13}$ , two-sample Kolmogorov-Smirnov test), including the median burst length (before V1 suppression:  
143 median 2 sp/burst, n = 835 bursts; during V1 suppression: median 3 sp/burst, n = 1739 bursts,  $p = 1.7 \times 10^{-18}$ , Mann-Whitney  
144 U test; **Figure 2g, inset**). Both the decrease in firing rates as well as the subsequent increase in burst spike ratio and burst  
145 length are consistent with the interpretation that, in the absence of stimulus drive, V1 suppression resulted in a removal of  
146 feedback-mediated excitation. Such removal of excitation would hyperpolarize dLGN cells, resulting initially in fewer action  
147 potentials and later ( $\geq 100$  ms) in bursting, given the hyperpolarization-mediated de-inactivation of T-type calcium channels.  
148 T-type calcium channels, abundant in thalamus, mediate low-threshold calcium spikes, whose amplitude is inversely related to  
149 membrane potential and is correlated to the number of action potentials in a burst riding its crest<sup>57</sup>.

150 Complementary to the results of global V1 suppression, we found that photoactivation of L6CT neurons in size 0 deg  
151 conditions (i.e., absence of sensory stimulation) was sufficient to promote tonic firing in dLGN (**Figure S2**). Indeed, activating  
152 CT feedback decreased the ratio of spikes fired in burst (before: 9.04%, during: 3.75%; n = 139 neurons;  $p = 1.7 \times 10^{-7}$ ,  
153 Wilcoxon signed-rank test) and shifted the distribution of spikes per burst towards lower values ( $p = 7.8 \times 10^{-5}$ , two-sample  
154 Kolmogorov-Smirnov test). However, unlike during global V1 suppression, we did not find that activation of L6CT neurons  
155 significantly affected firing rates (during: 4.2 sp/s vs. before: 2.7 sp/s; n = 167 neurons;  $p = 0.4$ , Wilcoxon signed-rank test),

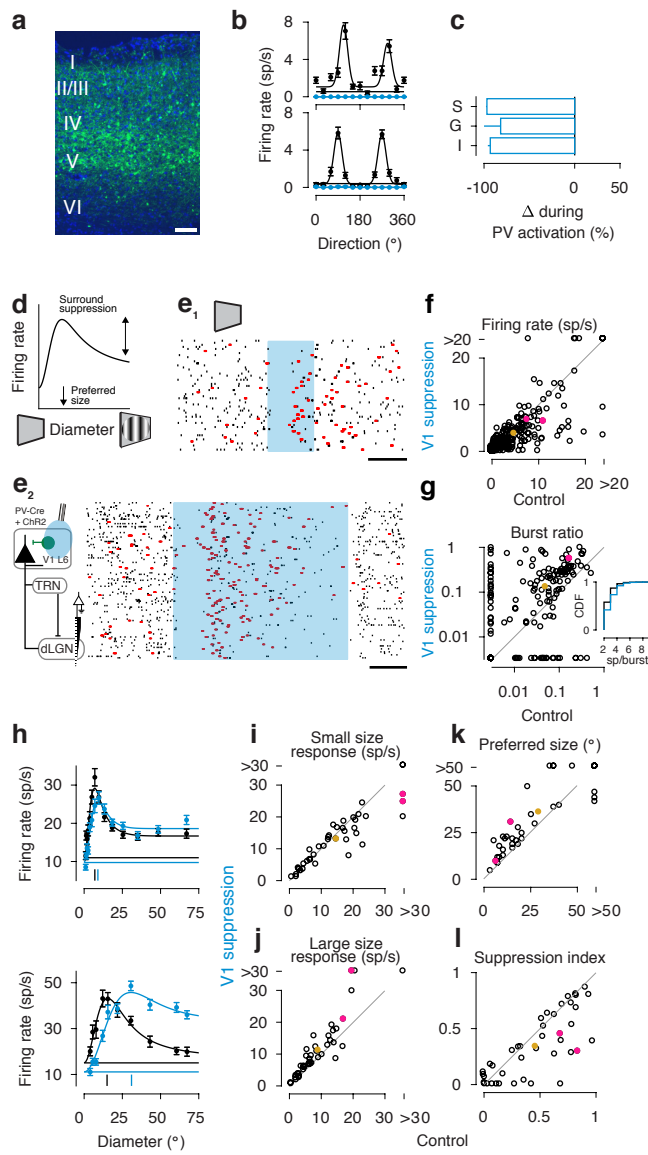


**Figure 2** Suppression of cortical feedback modulates responses in dLGN in a size-dependent manner.

(a) Coronal section of V1 of a PV-Cre mouse injected with cre-dependent AAV-ChR2. Green: ChR2-YFP, blue: DAPI. Scale bar 100  $\mu$ m. (b) Example direction tuning curves of neurons located in supragranular (top) or infragranular (bottom) layers during V1 suppression (blue) and control conditions (black). (c) Percent response change for cells in supragranular (S, n = 52), granular (G, n = 50) and infragranular (I, n = 82) layers, as determined by CSD<sup>58</sup>. All  $p < 5.1 \times 10^{-3}$ , Wilcoxon signed-rank test. (d) Schematic size tuning curve. (e) Recordings from dLGN. Responses of two example dLGN neurons to gray screen (size 0 deg) aligned to V1 suppression (shaded blue). Red: burst spikes, black horizontal bar: 200 ms. (e<sub>1</sub>) n = 54 trials, (e<sub>2</sub>) n = 105 trials. (f) Firing rates during vs. before V1 suppression. n = 276 neurons;  $p = 1.5 \times 10^{-5}$ , Wilcoxon signed-rank test. (g) Ratio of burst spikes during vs. before V1 suppression. n = 232 neurons;  $p = 4.1 \times 10^{-11}$ , Wilcoxon signed-rank test. Data points at marginals represent neurons whose burst ratio was 0. Inset: cumulative distribution of burst lengths during (blue) vs. before (black) V1 suppression ( $p = 3.6 \times 10^{-13}$ , two-sample Kolmogorov-Smirnov test). (h) Size tuning curves of two dLGN example neurons. Small vertical bars indicate preferred size; straight horizontal lines indicate response to blank screen (size 0 deg). Blue: V1 suppression, black: control condition. (i-l) Comparison of V1 suppression to control conditions for (i) responses to small sized stimulus ( $p = 0.0048$ ), (j) responses to large sized stimulus ( $p = 0.0013$ ), (k) preferred size ( $p = 5.1 \times 10^{-5}$ ), and (l) suppression index (SI) ( $p = 0.00038$ ), all Wilcoxon signed-rank test, n = 41 neurons. (b, c, h): Error bars: standard error of the mean (s.e.m). (e, g, i-l): pink: example neurons, gold: population mean. In panel (g), markers of the two example neurons almost completely overlap.

156 as effects of Ntsr1+ activation on the firing of individual dLGN neurons were diverse. This diversity is consistent with the  
157 interpretation of our functional mapping experiments, where we also observed a mix of enhancement and suppression for  
158 dLGN neurons with “near” RFs (**Figure 1k**). Together, in the absence of visual stimuli, CT feedback seems to exert its effect  
159 mainly through the direct, excitatory pathway, boosting firing rates and promoting tonic firing mode.

160 We next presented drifting gratings of various sizes centered on the RF of each dLGN neuron and recorded responses while  
161 interleaving trials with and without optogenetic suppression of V1 (**Figure 2h-l**). Consistent with our findings presented in  
162 **Figure 2e-f**, for blank stimuli, we observed a  $\sim 10\%$  decrease in firing rates (control: 5.4 sp/s vs. V1 suppression: 4.5 sp/s,  
163  $n = 41$ ;  $p = 0.0043$ , Wilcoxon signed-rank test) and an increase in burst ratio (control: 0.08 vs. 0.15,  $n = 41$ ; 0.0195, Wilcoxon  
164 signed-rank test). We then fit each dLGN cell’s responses to gratings of various sizes under either the control or V1 suppression  
165 condition with a descriptive model of size tuning (ratio of Gaussians model, RoG)<sup>59</sup>, defining relative contributions of an  
166 excitatory center and inhibitory surround, to obtain a size-tuning curve (**Figure 2d, h**). From this fit, we determined the  
167 preferred size as the size eliciting the maximum response, and the suppression strength as an index (SI) quantifying the response  
168 to the surround relative to the center, with 0 indicating no suppression and 1 indicating full suppression.

169 In order to probe the effects of cortical feedback on spatial integration, we first asked if V1 suppression differentially  
170 affected dLGN spiking responses to drifting gratings according to stimulus size. For small stimuli (i.e., those closest to the  
171 preferred size during the control condition), we observed, similar to our results on spontaneous activity, that V1 suppression  
172 caused a decrease in dLGN responses (control: 5.4 sp/s vs. V1 suppression: 4.5 sp/s,  $n = 41$  neurons;  $p = 0.0043$ , Wilcoxon  
173 signed-rank test; **Figure 2i**). However, for the largest presented size, we found in accordance with results from<sup>40</sup> the opposite  
174 effect: increased dLGN responses during V1 suppression (control: 9.3 sp/s vs. V1 suppression: 11.1 sp/s,  $n = 41$ ;  $p = 0.0013$ ,  
175 Wilcoxon signed-rank test; **Figure 2j**). Hence, our results indicate that cortical feedback can affect dLGN responses in a  
176 contextual manner, enhancing responses to the preferred size while suppressing responses to larger stimuli. To probe if the  
177 size-dependent modulation of dLGN firing rates during V1 suppression translated into significant changes in spatial integration,  
178 we next examined the size tuning curves of individual cells. Indeed, we found that during V1 suppression, dLGN neurons  
179 preferred larger sizes (control: 29.9 deg vs. V1 suppression: 35.4 deg;  $n = 41$ ;  $p = 1.2 \times 10^{-5}$ , Wilcoxon signed-rank test;  
180 **Figure 2k**), and were less surround-suppressed (control: 0.47 vs. V1 suppression: 0.34;  $n = 41$ ;  $p = 0.00038$ , Wilcoxon  
181 signed-rank test; **Figure 2l**).

182 While V1 suppression did not abolish surround suppression in dLGN (28/41 cells still had  $SI \geq 0.1$ ), our results indicate  
183 a substantial involvement of cortical feedback in shaping spatial integration in dLGN: feedback enhances contextual effects,  
184 facilitating responses to the center while suppressing those to the surround, resulting in sharper RFs and a stronger center-  
185 surround antagonism. While the enhanced small-size responses are consistent with a net depolarizing effect of CT feedback,  
186 the increased surround suppression for large sizes is suggestive of CT feedback acting via inhibition.

187 **Capturing effects of feedback on dLGN spatial integration requires wide CT inhibition in a firing rate model**  
188 How could CT feedback shape dLGN spatial integration via inhibition? We first investigated this question by exploiting a  
189 previously developed mechanistic firing rate model of dLGN, the extended difference-of-Gaussians model (eDoG)<sup>60,61</sup>. In the  
190 eDOG model (**Figure 3a**), the response of a dLGN relay cell ( $R$ ) arises from excitatory and inhibitory feedforward input from  
191 retinal ganglion cells ( $G$ ), whose RF is described by a difference-of-Gaussians model<sup>62</sup>, and excitatory and inhibitory feedback  
192 input from a population of cortical neurons ( $C$ ) with various orientation preferences (**Figure 3a**). The connections between the  
193 three processing stages are represented by 2D Gaussian spatial coupling kernels ( $K$ ), whose amplitude captures the synaptic  
194 strength, and whose width captures the spatial scale, over which visual information is integrated. The model is segregated  
195 into an ON and OFF pathway, where feedforward input is pathway-specific, while cortical feedback is pathway-unspecific  
196 (cross-symmetric), arising from both ON and OFF pathways. We adjusted the model’s parameters to reflect known properties  
197 of the mouse visual system (**Table S1**). While the model is agnostic to the source of feedback-mediated inhibition, it allows  
198 exploration of how the spatial scale of inhibitory feedback shapes dLGN spatial integration.

199 To explore how inhibition via CT feedback could increase surround suppression and sharpen RFs of dLGN neurons, we  
200 systematically varied the width of the inhibitory feedback coupling kernel (**Figure 3b, top**) and simulated tuning curves for  
201 grating patches of different sizes with and without CT feedback (**Figure 3b, bottom**). Setting the width parameter of the  
202 inhibitory CT feedback kernel to equal the width of the excitatory CT feedback kernel ( $\sigma_{inh\ fb} = \sigma_{exc\ fb}$ ), the model failed to  
203 replicate our experimentally observed results (**Figure 3b<sub>1</sub>**): CT feedback had an overall suppressive effect, reducing responses

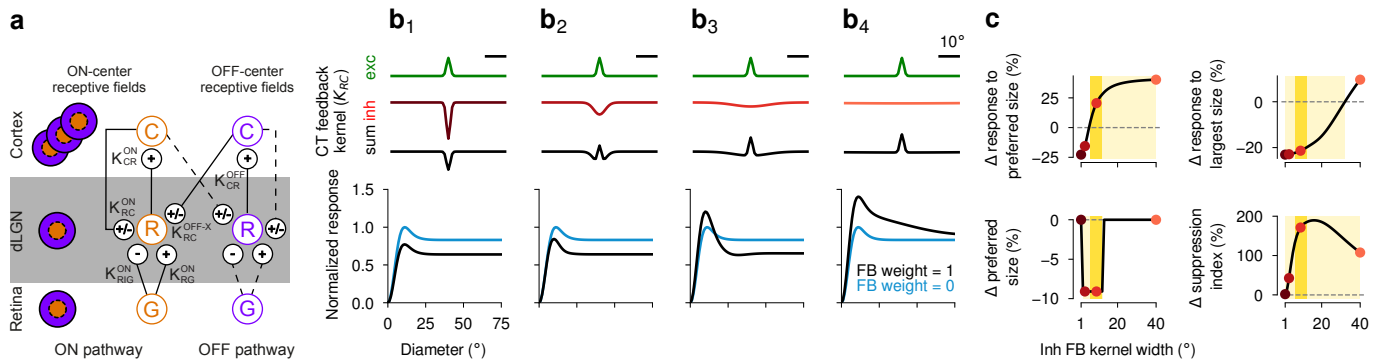


**Figure 3** Wide inhibitory feedback coupling kernel is necessary to predict feedback-enhanced surround suppression and sharpening of RFs in dLGN.

**(a)** Schematic of the extended difference-of-Gaussians model (eDOG). In the eDOG model, center-surround RFs of dLGN relay cells ( $R$ ) are modelled by feedforward inputs from retinal ganglion cells (RGCs,  $G$ ) and feedback inputs from cortex ( $C$ ). The three layers are connected by 2D Gaussian coupling kernels ( $K$ ). RGCs, whose RFs are described by a difference-of-Gaussians model, provide excitatory ( $K_{RG}$ ) and inhibitory ( $K_{RIG}$ ) feedforward input to relay cells. CT feedback of both signs ( $K_{RC}$ ) originates from a population of cortical cells, which in turn receive input from dLGN relay cells ( $K_{CR}$ ). While the feedforward pathway is segregated into an ON and OFF pathway, CT feedback is cross-symmetric, meaning that e.g. ON center relay cells receive excitatory and inhibitory feedback from cortical ON and OFF cells. Although cortical cells are orientation tuned, a given relay cell receives input from a diverse population of cortical cells, making the net effect of CT feedback insensitive to the orientation of the stimulus. Adapted from Mobarhan et al. (2018)<sup>61</sup>. **(b)** Results of varying the width of the inhibitory CT feedback coupling kernel on simulated size tuning curves. *Top*: Excitatory (green), inhibitory (red) CT feedback coupling kernels, and their sum (black). **(b<sub>1</sub>)** Same width ( $\sigma_{inh\ fb} = \sigma_{exc\ fb}$ ), **(b<sub>2</sub>)** same width as inhibitory feedforward kernel ( $\sigma_{inh\ fb} = \sigma_{inh\ ff}$ ), **(b<sub>3</sub>, b<sub>4</sub>)** two larger widths (**b<sub>3</sub>**:  $\sigma_{inh\ fb} = 9 \times \sigma_{exc\ fb}$ ; **b<sub>4</sub>**:  $\sigma_{inh\ fb} = 40 \times \sigma_{exc\ fb}$ ). Note that the area under the curve is the same for all inhibitory feedback coupling kernels. *Bottom*: simulated dLGN size tuning curves with cortical feedback intact (black) and abolished (blue). For each width, responses are normalized to the peak response in the condition without CT feedback. **(c)** Effects of CT feedback for kernel widths between 1 deg and 40 deg in 1 deg steps on response magnitude to the preferred stimulus size (*top left*), response magnitude to the largest stimulus (*top right*), the preferred size (*bottom left*), and surround suppression (*bottom right*), revealed by zeroing the weight of CT feedback. Red points correspond to example kernel widths depicted in (b). Parameter range in which simulations render qualitatively similar results as in experimental observations, with regards to each single variable (*light yellow*) vs. all four variables (*dark yellow*). Light yellow ranges correspond to  $6 \text{ deg} \leq \sigma_{inh\ fb} \leq 40 \text{ deg}$  (response to preferred size),  $1 \text{ deg} \leq \sigma_{inh\ fb} \leq 32 \text{ deg}$  (response to largest size),  $2 \text{ deg} \leq \sigma_{inh\ fb} \leq 12 \text{ deg}$  (preferred size),  $1 \text{ deg} \leq \sigma_{inh\ fb} \leq 40 \text{ deg}$  (suppression index). Dark yellow range corresponds to  $6 \text{ deg} \leq \sigma_{inh\ fb} \leq 12 \text{ deg}$ .

for all stimulus sizes (22.8% decrease for preferred stimulus size; 23.1% decrease for largest stimulus size), and failed to substantially alter the preferred stimulus size and surround suppression (1.9% increase). We next increased the spatial scale of inhibitory CT feedback to match the spatial scale of feedforward inhibition ( $\sigma_{inh\ fb} = \sigma_{inh\ ff}$ , **Figure 3b<sub>2</sub>**). While now CT feedback started to decrease the preferred size (9.1% decrease) and increase surround suppression (42.7% increase), CT feedback still led to overall weaker responses, even for small sizes (15.6% decrease for preferred stimulus size; 22.9% decrease for largest stimulus size). Only when the width of the inhibitory CT feedback component was sufficiently large ( $\sigma_{inh\ fb} = 9 \times \sigma_{exc\ fb}$ ; **Figure 3b<sub>3</sub>**), our simulations rendered a pattern comparable to the size-dependent effects observed in the experimental data: while responses to the preferred stimulus size were enhanced (20.6% increase), responses to the largest stimulus size were suppressed (21.4% decrease). In accordance with the experimental data, we also observed that CT feedback decreased the preferred size (9.1% decrease) and strengthened surround suppression (171.2% increase). Finally, when we further increased the spatial scale of the inhibitory feedback kernel ( $\sigma_{inh\ fb} = 40 \times \sigma_{exc\ fb}$ ; **Figure 3b<sub>4</sub>**), CT feedback increased firing rates independent of stimulus size (40.4% increase for preferred stimulus size; 9.7% increase for largest stimulus size), enhanced surround suppression (107.7% increase), but did not affect the preferred stimulus size (0.0% change).

A summary of simulations with more complete variation of the width of the inhibitory CT feedback kernel revealed that feedback-induced amplification of responses to the preferred size (**Figure 3c**, top left, light yellow) and strengthening of

219 surround suppression (**Figure 3c**, lower right, light yellow) required sufficiently wide kernels. Much wider kernels, however,  
220 failed to reproduce the feedback-induced decrease of responses to larger stimulus sizes (**Figure 3c**, top right, light yellow) and  
221 sharpening of RFs (**Figure 3c**, lower left, light yellow), restricting the parameter range that replicated experimental results to  
222 larger but spatially confined inhibitory feedback kernel widths (**Figure 3c**, dark yellow). Taken together, the model suggests  
223 that cortical feedback enhances contextual effects in dLGN via an inhibitory component that integrates information over a  
224 sufficiently large, yet still localized, spatial scale.

## 225 **RF properties of mouse visual TRN are suited for providing wide-scale inhibition to dLGN**

226 A candidate circuit through which cortex could provide wide-scale inhibitory influence over dLGN is indirect inhibition via the  
227 visual TRN (visTRN). Present in all mammals, the TRN is a sheath of GABAergic neurons surrounding the lateral and anterior  
228 part of the thalamus<sup>63,64</sup>. Since TRN receives input from axon collaterals of both thalamic relay cells and cortico-thalamic  
229 neurons, it is in a prime position to modulate the flow of information between the thalamus and the cortex<sup>63,64</sup>. Owing to its  
230 inhibitory projections to dLGN, visTRN has been considered a “guardian of the gate to cortex”<sup>65</sup>, and has been implicated in  
231 gain control<sup>65,66</sup> and attentional selection<sup>67–71</sup>. To explore whether CT feedback might enhance surround suppression in dLGN  
232 via visTRN, we first tested whether mouse visTRN neurons have appropriate feature selectivity, i.e. large RFs, responses that  
233 increase with stimulus size, and little surround suppression.

234 We recorded from visTRN (**Figure 4**) by lowering a silicon probe at appropriate stereotaxic coordinates to a depth of  
235 ~ 3500  $\mu$ m (**Figure 4a**), until we found neurons with vigorous, visually evoked responses. Since visTRN is located near other  
236 thalamic nuclei with visually responsive neurons, we *post-mortem* confirmed via retrograde viral labeling that our visTRN  
237 recording sites were in the vicinity of neurons providing input to dLGN (**Figure 4b**). Indeed, after injection of rAAV2/retro-  
238 CMV-GFP<sup>72</sup> into dLGN (**Figure 4b**<sub>1</sub>), we found dense GFP expression in the dorsocaudal part of TRN, corresponding to the  
239 visual sector<sup>63,71</sup> (**Figure 4b**<sub>2</sub>). Closer inspection revealed retrogradely labeled cell bodies, localized near the DiI-labeled  
240 electrode track (**Figure 4b**<sub>3</sub>). This histological evidence, in combination with the robust visual responses encountered during  
241 our recordings, demonstrates that we indeed targeted visTRN.

242 To test RF properties of mouse visTRN, we first mapped classical RFs of single visTRN neurons using a sparse noise  
243 stimulus and determined their size (**Figure 4c, d**). RF sizes of visTRN neurons covered a wide range, with individual neurons  
244 displaying small (**Figure 4c**, *second from the right*: (area = 169.3  $\text{deg}^2$ ;  $R^2 = 0.92$ ) or large RFs (**Figure 4c** *rightmost*:  
245 (area = 780.5  $\text{deg}^2$ ;  $R^2 = 0.84$ ). Comparing sizes of the classical RFs in visTRN ( $n = 218$  neurons;  $566.1 \pm 37.4 \text{ deg}^2$ ;  
246 mean  $\pm$  s.e.m.) to a population of dLGN neurons measured under the same conditions ( $n = 197$ ;  $75.9 \pm 5.1 \text{ deg}^2$ ) revealed  
247 that, despite having overlapping distributions, classical RFs of visTRN neurons were on average  $7.5 \times$  larger ( $p = 1.0 \times 10^{-51}$ ,  
248 Mann-Whitney U test, **Figure 4c,d**) and more variable in size ( $p = 8.3 \times 10^{-23}$ , Brown-Forsythe test). Next, centered on the  
249 RFs, we presented drifting gratings of various sizes and fit the trial-averaged responses with the RoG model (**Figure 4e-h**).  
250 Analogously to our analysis of dLGN size tuning, we used the model fit to determine, for each visTRN neuron, its preferred size  
251 and strength of surround suppression. Similar to the example neuron (SI: 0.02, **Figure 4e, f**), the majority of visTRN neurons  
252 experienced little to no surround suppression ( $n = 125$  neurons; mean SI:  $0.17 \pm 0.02$ , **Figure 4g, h**). In fact, almost half of  
253 the population (48.8%) had a SI that was weaker than 0.05. Thus, similar to neurons in visTRN in carnivores and primates  
254 (perigeniculate nucleus)<sup>73–77</sup>, mouse visTRN neurons have spatially localized, yet large RFs and experience little surround  
255 suppression. By exerting weak inhibition during presentation of small stimuli and strong inhibition during presentation of large  
256 stimuli, the properties of visTRN neurons are well suited for sculpting surround suppression in dLGN.

## 257 **Suppressing cortical feedback increases preferred size and reduces responses in visTRN, in particular for 258 large stimuli**

259 If CT feedback indeed enhanced dLGN surround suppression by recruiting inhibition from visTRN, then how should CT  
260 feedback modulate visTRN responses? We made three specific predictions: (1) If CT feedback provided substantial indirect  
261 inhibition via visTRN, V1 suppression should reduce visTRN responses. (2) If visTRN was involved in CT feedback-mediated  
262 sharpening of dLGN RFs, V1 suppression should increase preferred size in visTRN, shifting the peak of inhibition transmitted  
263 to dLGN to larger stimulus sizes. (3) If CT feedback enhanced surround suppression in dLGN via inhibition from visTRN,  
264 visTRN responses during V1 suppression should be reduced most for larger stimuli.

265 To test these hypotheses, we measured responses of visTRN neurons in PV-Cre mice to stimuli of varying size, with  
266 interleaved trials in which we suppressed CT feedback by photoactivating PV+ inhibitory interneurons in V1 (**Figure 5a**).

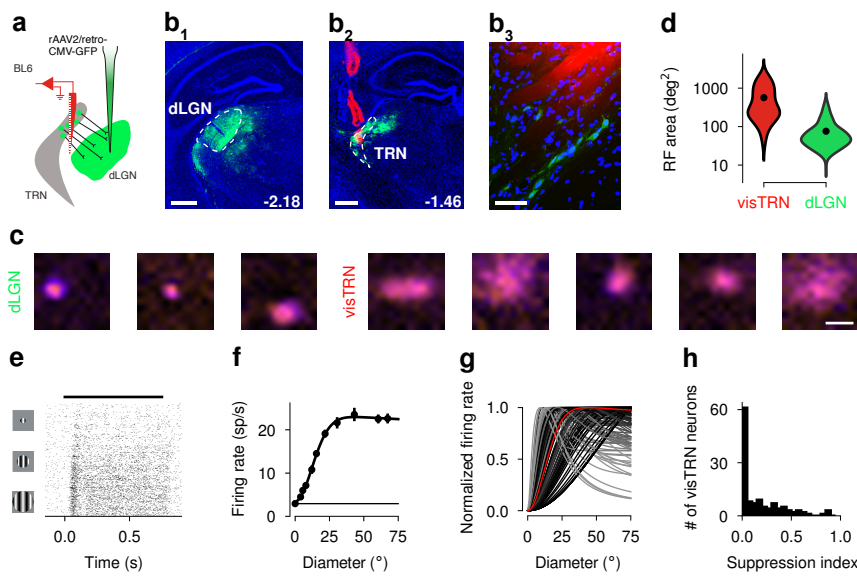


**Figure 4** Most neurons in visTRN have large RFs and experience little surround suppression.

(a) Schematic of viral labeling of visTRN neurons with GFP by injecting a retrograde AAV<sup>72</sup> into dLGN. (b) GFP labeling of visTRN in an example mouse. b<sub>1</sub>: dLGN injection site. Dashed outline: dLGN; scale bar: 0.5 mm. b<sub>2</sub>: visTRN recording site for the same mouse. Dashed outline: TRN; scale bar: 0.5 mm; numbers indicate distance from bregma in mm. b<sub>3</sub>: Magnified view around tip of electrode trace from slice shown in b<sub>2</sub>. Scale bar: 50  $\mu$ m. All panels: blue: DAPI, green: GFP, red: DiI labeled electrode trace. (c) Classical RF for three example dLGN neurons (left) and five example visTRN neurons (right). Orange: OFF response, purple: ON response, scale bar: 20 deg. (d) Comparison of classical RF sizes for recorded visTRN (n = 218) and dLGN (n = 197) neurons. Outlines indicate distribution of classical RF sizes. Black: mean;  $p = 1.0 \times 10^{-51}$ , Mann-Whitney U test. (e) Raster plot of an example visTRN neuron recorded in a size tuning experiment. Trials are sorted by stimulus size with lower rows showing responses to larger stimulus sizes. 50 trials per size; black horizontal bar: stimulus presentation period. (f) Size tuning curve corresponding to (e). Horizontal line: response to size 0 deg. Error bars: s.e.m.. (g) Size tuning curves for visTRN cell population (n = 125). Strength of surround suppression is represented by darkness of line. Red: example neuron from (e, f). (h) Distribution of suppression indices for recorded visTRN population.

267 When we inspected the raster plots (Figure 5b) and fitted size tuning curves (RoG model, Figure 5c) of single visTRN neurons,  
 268 we found that suppressing V1 reduced overall responsiveness. This reduction was robust not only for the example neuron  
 269 (-46.2%), but also for the population of recorded visTRN neurons (Figure 5d), where responses were reduced to approximately  
 270 half (V1 suppression:  $15.6 \pm 2.2$  sp/s; control:  $23.4 \pm 2.5$  sp/s; n = 67;  $p = 4.9 \times 10^{-10}$ ; Wilcoxon signed-rank test; Figure 5e).  
 271 We conclude from this substantial response reduction during V1 suppression that visTRN is strongly engaged by CT feedback.

272 To test our next hypotheses and investigate more specifically how CT feedback might change visTRN responses in a  
 273 size-dependent way, we inspected, for units that were still responsive during V1 suppression (mean firing rate  $\geq 0.1$  sp/s)  
 274 more closely the parameters of the fitted size tuning curves. In agreement with our second hypothesis, V1 suppression did  
 275 indeed increase visTRN preferred size by about 20% (V1 suppression:  $45.8 \pm 2.9$  deg; control:  $38.5 \pm 2.7$  deg; n = 61 neurons;  
 276  $p = 0.001$ ; Wilcoxon signed-rank test; Figure 5f). This increase indicates that visTRN's peak inhibitory output to dLGN might  
 277 shift towards larger stimulus sizes, which in turn could explain why during V1 suppression we observe broadened dLGN  
 278 receptive fields (Figure 2k).

279 While CT feedback did not change the strength of surround suppression in visTRN (SI V1 suppression:  $0.15 \pm 0.03$ ; control:  
 280  $0.18 \pm 0.03$ ; n = 61;  $p = 0.18$ ; Wilcoxon signed-rank test; Figure 5g), we found that modulation of visTRN responses by  
 281 CT feedback nevertheless depended on stimulus size. Inspecting the differences in normalized firing rates of the fitted size  
 282 tuning curves, we found that responses to larger stimuli were more strongly affected by V1 suppression than responses to the  
 283 smallest stimuli (Figure 5h; see also Figure 5d). In the range of 0 deg to 18 deg, expanding the stimulus size by 1 deg led to a  
 284 significant increase of the effect of V1 suppression (n = 63;  $p < 0.05$ ; bootstrap test; Figure 5h). Hence, in agreement with  
 285 our third hypothesis, while CT feedback seems to enhance visTRN responses across all stimulus sizes, this enhancement is  
 286 progressively stronger with increasing stimulus size until approaching an asymptote.

What is the nature of the transformation exerted by CT feedback on visTRN responses? If V1 suppression had reduced visTRN responses independent of stimulus size and thus independent of the visTRN activity level, the effect would be best explained by a subtractive mechanism. However, since V1 suppression was more effective for large stimuli, which in control conditions evoked the strongest response, the effect might instead be based on a divisive mechanism. To test this, we fit a threshold-linear model (Figure 5i, blue), which predicts responses during V1 suppression by shifting and scaling responses in the control condition; because V1 suppression cannot lead to negative firing rates, the model additionally zeroes firing rates up to a threshold for activation. Although it is impossible for this simple model to capture the observed changes in preferred size, it captured the effects of V1 suppression on size tuning curves reasonably well for the majority of visTRN neurons (46/63 neurons,  $R^2 \geq 0.8$ ). Focusing on this subset of well-fit neurons, where V1 suppression had mostly linear effects, we found for both the example neuron shown in Figure 5i ( $R^2 = 1$ ; threshold: 0.15; slope: 0.74; same neuron as in Figure 5b,c) as well as the recorded population (Figure 5j) a mild subtractive effect (threshold:  $0.06 \pm 0.04$ , mean  $\pm$  s.e.m.;  $p = 0.04$ , Wilcoxon signed-rank test) and a substantial and consistent divisive effect (slope:  $0.65 \pm 1.13$ ;  $p = 2.8 \times 10^{-5}$ , Wilcoxon signed-rank test; Figure 5j). Since divisive scaling implies that high firing rates are reduced most, and visTRN neurons have high responses to large stimuli (see Figure 4e-h), this analysis further corroborates our finding that CT feedback most strongly engages visTRN activity in response to large stimuli. Such size-dependent recruitment of inhibition via visTRN by CT feedback might account for our earlier finding that dLGN responses to large stimuli are enhanced when CT feedback is suppressed (Figure 2j). Taken together, the substantial modulation of visTRN responses by CT feedback, and the size-dependent recruitment of visTRN by CT feedback, make visTRN an ideal candidate for mediating feedback-enhanced surround suppression in dLGN.

## Discussion

Using a combination of viral tracing, bi-directional optogenetic manipulations, and computational modeling, we show that one role of cortical feedback to mouse dLGN is to sculpt spatial integration by sharpening geniculate RFs and enhancing surround suppression. We identified spatially specific, distant suppressive influences of corticothalamic feedback, which are most consistent with arising from indirect inhibition. Guided by simulations in our thalamo-cortical network model, which indicated that wide-scale inhibitory CT feedback was required to reproduce our experimentally observed results, we show that the spatial selectivity of neurons in visTRN and their size-specific recruitment by CT feedback makes them an ideal candidate for mediating feedback-enhanced surround suppression in dLGN. Therefore, corticothalamic feedback, likely with the involvement of TRN, sharpens spatial responses and strengthens contextual modulations in dLGN.

### Spatial integration in dLGN

Spatial integration in dLGN is shaped by multiple mechanisms, as surround suppression occurs both up- and downstream of dLGN. Indeed, it is first established in the retina<sup>78-80</sup>, and it is also a hallmark of responses in area V1<sup>81-87</sup>. The mechanisms for surround suppression in dLGN therefore include inheritance from feedforward retinal input<sup>32,88</sup>, augmentation via non-linearities at the retino-geniculate relay<sup>89</sup>, recurrent thalamic inhibition<sup>90,91</sup>, and CT feedback<sup>34,35,37,39,92</sup>. The CT feedback-mediated sharpening of RFs and strengthening of the center-surround antagonism we observed in dLGN of awake mice parallels previous results in anesthetized cats<sup>34,36,37</sup>, ferrets<sup>38</sup>, and non-human primates<sup>33,35,39</sup>.

The modulations of geniculate spatial integration we observed could arise from differential, size-dependent recruitment of a more narrow, direct excitatory, and a wider, indirect inhibitory CT feedback component, with the balance shifting towards direct excitation for small stimuli and towards indirect inhibition for large stimuli. The wide band of suppressive influences revealed in our functional CT circuit mapping experiments, the requirement of a wide inhibitory feedback coupling kernel in our model, and our recordings of response properties in visTRN are consistent with differential, size-dependent recruitment of CT feedback. It will be interesting to see in future studies whether stimulus size is the only determinant of differential CT feedback recruitment, or whether other aspects of stimulus context known to influence surround suppression, such as the statistics of natural scenes<sup>93</sup>, might also play a role.

### Role of TRN

By measuring visTRN RF properties, their modulation by CT feedback, and by simulating the impact of inhibitory feedback at various spatial scales in a mechanistic dLGN model<sup>61</sup>, we found evidence that CT feedback can sculpt dLGN spatial integration via visTRN. While visTRN has long been implicated in powerfully controlling dLGN<sup>65</sup>, the specific form of this influence

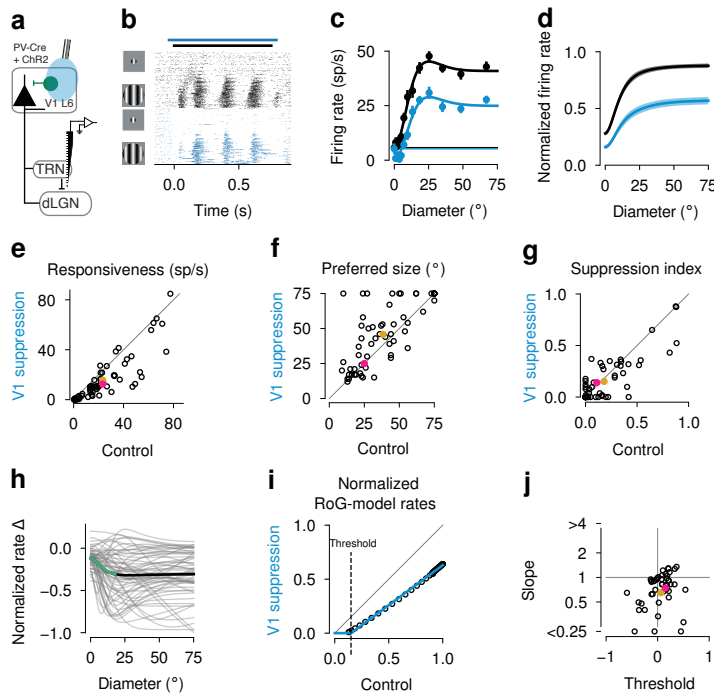


**Figure 5** Suppressing cortical feedback reduces activity and increases preferred stimulus size in visTRN.

(a) Schematic of experimental approach. (b) Raster plot of an example visTRN neuron recorded in a size tuning experiment. Trials are sorted by feedback condition and stimulus size with lower rows depicting responses to larger stimulus sizes (20 trials per size and feedback condition; black horizontal bar: stimulus presentation period; blue horizontal bar: V1 suppression period). (c) Size tuning curves, same example neuron as in (b) (horizontal bars: Response to size 0 deg; error bars: s.e.m.). (d) Mean of RoG fits for the visTRN population ( $n = 63$ ; shaded areas: s.e.m.). (e-g) Mean evoked response (e;  $n = 67$ ;  $p = 4.9 \times 10^{-10}$ ), preferred size (f;  $n = 61$ ;  $p = 0.001$ ), and suppression indices (g;  $n = 61$ ;  $p = 0.18$ ; Wilcoxon signed-rank test) for visTRN cell population. (h) Difference between ratio of Gaussians model for V1 suppression and control conditions (gray: single visTRN neurons; black: population mean; green: range in which expanding the stimulus size by 1 deg led to a significant increase of the effect (0 deg - 18 deg;  $p < 0.05$ ; bootstrap test;  $n = 63$ ). (i) Threshold linear fit (blue) to RoG model evaluated at 1 deg steps (black) for example visTRN neuron from (b, c) (slope: 0.74; threshold: 0.15;  $R^2 = 1$ ). (j) Slope ( $p = 2.8 \times 10^{-5}$ ) and threshold ( $n = 46$ ;  $p = 0.04$ , Wilcoxon signed-rank test) parameters extracted from threshold linear fits for visTRN population. Panels (b-d): blue: V1 suppression; black: control; Panels (e-g, j): pink: example neuron; gold: population mean.

333 has been a matter of debate. A role in shaping dLGN spatial integration would oppose one of the two prevailing theories of  
 334 TRN function, the “thermostat hypothesis”<sup>65</sup>, according to which TRN’s role is to homogenize dLGN activity through negative  
 335 feedback. The “searchlight hypothesis”, on the other hand, postulates that strong inhibition mediated by bursting visTRN cells  
 336 can focally trigger re-bound excitation in dLGN, resulting in enhanced spatial selectivity<sup>65</sup>. Although our results suggest a  
 337 similar role of visTRN for early visual processing, they speak more in favor of a “dual component searchlight”, where dLGN  
 338 spatial selectivity is enhanced by direct, localized excitation from L6CT cells acting in concert with indirect, widespread  
 339 inhibition from visTRN.

340 An alternative source of indirect inhibition in dLGN are local interneurons, which make up  $\sim 5\%$  of mouse dLGN<sup>94</sup> and  
 341 whose connectome allows participation in a mix of global and local inhibitory processing<sup>95</sup>. In favor of local influences are  
 342 studies in cats, which have shown that dLGN interneurons are sensitive to polarity, being organized into concentric subunits of  
 343 opposite sign<sup>96</sup>, and provide dLGN relay cells with either specific opposite-sign (“push-pull”) or same-sign inhibition<sup>96,97</sup>.  
 344 Such specific inhibition is thought to predominantly shape aspects of the relay cells’ classical RF<sup>97</sup>. In contrast to our findings  
 345 in visTRN, RFs of murine dLGN interneurons seem to have sizes comparable to relay cells<sup>98</sup>, which would enable a role in  
 346 specific, local inhibition. That said, since signaling in dLGN interneurons can happen via dendrites without depolarization  
 347 of the cell body<sup>99</sup>, the RF size of dLGN interneurons measured as spiking output will likely only represent a subset of the  
 348 spatial filtering operations that this neuron type can perform. To disentangle the relative contribution of dLGN interneurons

349 and visTRN to feedback-enhanced surround suppression in dLGN, targeted recordings from geniculate interneurons, and an  
350 assessment of their modulation by CT feedback will be a crucial next step.

351 Our finding that V1 suppression yielded modulatory influences of firing rate in dLGN, while substantially reducing visTRN  
352 responses sheds further light onto the role of cortical vs. subcortical inputs for these two thalamic nuclei. Our estimation of a  
353 ~ 50% V1 contribution to visTRN firing rates during size tuning fits observations in slice preparations preserving corticothalamic  
354 connectivity, where EPSPs elicited by stimulation of L6CT neurons are stronger in TRN than in relay neurons<sup>100,101</sup>. How  
355 does this knowledge from slice physiology translate to *in vivo* studies? While L6CT pyramidal cell's inputs to dLGN are  
356 clearly modulatory<sup>16,41</sup>, the results in visTRN are more mixed. Similar to our results, some studies had already noted a strong  
357 reduction of visTRN activity during CT feedback suppression via cooling<sup>102</sup>, ibotenate lesions<sup>103</sup> or optogenetic activation of  
358 PV+ interneurons<sup>42</sup>; others, however, observed no changes of visTRN responses after removal of CT feedback, and therefore  
359 concluded that visTRN was mainly driven by subcortical inputs<sup>77,104</sup>. A possible explanation for this discrepancy might be that  
360 in anesthetized animals the effects of CT feedback on visTRN responses have been underestimated, because the responsiveness  
361 of feedback projections<sup>105</sup>, including CT feedback<sup>24</sup>, might be particularly reduced during anesthesia, and attentional processes  
362 adding to the normal recruitment of CT feedback are lacking<sup>71,103</sup>.

363 Our findings about the role of CT feedback in shaping dLGN spatial integration could be extended by considering the  
364 time course of effects. Indeed, both for the modeling part as well as for the experimental results, we focused in this study on  
365 time-averaged responses. We made this choice because L6CT feedback is known to have a wide range of axonal conduction  
366 latencies, including very short ones<sup>106</sup>, with feedback effects arriving in dLGN while its feedforward response is still unfolding.  
367 Since latencies might not only vary between different types of L6CT neurons<sup>106</sup>, but might also be subject to global trial-by-trial,  
368 state-dependent modulations<sup>107</sup>, the most powerful approach to tackling this question would be simultaneous dual- or multi-area  
369 recordings within the thalamo-cortico-thalamic loop.

## 370 Manipulating cortico-thalamic feedback

371 To probe the effects of CT feedback, we suppressed cortical activity by optogenetic activation of V1 PV+ inhibitory interneurons.  
372 Relying on intracortical inhibition, this method provides strong suppression; its global character, however, limits the specificity  
373 with which individual circuits can be targeted<sup>108</sup>. In the case of CT feedback, global V1 suppression might not only modulate  
374 thalamic activity via the L6CT circuit, but also via other, polysynaptic pathways. One such potential alternative route could  
375 arise from layer 5 corticofugal neurons, known to influence the gain of responses in superior colliculus (SC)<sup>109,110</sup>, which  
376 in turn provides excitatory, driving input to dLGN<sup>111</sup>. We think that it is unlikely that effects observed in our study were  
377 mediated via the SC. First, effects of direct SC suppression on dLGN responses are limited to the most dorsal 150 $\mu$ m of  
378 dLGN<sup>112</sup>, while effects evoked by V1 suppression in our study spanned the entire depth of dLGN. Second, suppressing V1  
379 affects SC responses independently of stimulus size<sup>110</sup>, inconsistent with the size-dependent effects we found for dLGN. To  
380 rule out the effects of polysynaptic circuits during global suppression, it is not sufficient to instead selectively suppress L6CT  
381 pyramidal cells at the level of V1, because they have an intracortical axon collateral targeting layer 5<sup>53</sup> and make privileged  
382 connections to a L6, translaminar PV+ interneuron subtype<sup>52,54</sup>, which strongly regulates the gain of the entire V1 column (see  
383 also **Figure S2c**)<sup>40,52,54</sup>. Instead, a decisive next step would be to directly suppress axon terminals of L6CT pyramidal cells at  
384 the thalamic target. This is challenging because direct optogenetic inhibition of axon terminals is prone to unintended excitatory  
385 effects<sup>108,113</sup>, due to changes in pH in case of light-driven proton pumps<sup>114</sup>, or due to a depolarizing reversal potential for  
386 chloride in case of anion-selective channelrhodopsins (ACRs)<sup>108</sup>. Complicating matters further, while the Ntsr1-Cre mouse line  
387 gives selective access to L6CT pyramidal cells<sup>44,52-54</sup>, it is known that the targeted population is not homogeneous but contains  
388 at least 2 subtypes defined by morphology<sup>54,115,116</sup>, 4 subtypes defined by electrophysiology and morphology<sup>116</sup>, and 4 major  
389 subtypes defined by transcriptomics<sup>115,116</sup>. It is currently unknown to which degree these subtypes differentially contribute to  
390 CT feedback modulations.

391 Our results contribute to an emerging view according to which manipulation of L6CT pyramidal cells does not simply  
392 produce global gain changes in dLGN, and photostimulation and photosuppression do not simply produce changes with opposite  
393 sign. First, effects of L6CT activation, as shown here and consistent with previous studies<sup>26,117</sup>, cannot be described by a  
394 global gain factor, because these effects have a spatial profile, ranging from a mix of suppression and facilitation at the dLGN  
395 region covering the retinotopic location of the L6 source, to suppression beyond. Second, synapses in the CT feedback circuit  
396 to first-order thalamus are facilitating in case of the direct excitatory pathway, and depressing in case of the indirect inhibitory

397 pathway via TRN, rendering the net effect of L6CT neurons on relay cells dependent on firing frequency<sup>25</sup>. Although this  
398 frequency-dependence is likely to be relevant for interpreting CT feedback effects *in vivo*<sup>118</sup>, the lack of targeted recordings in  
399 awake, behaving animals, and the notoriously low firing rates of L6CT neurons<sup>51,119–126</sup> make it difficult to predict how this  
400 frequency-dependence will modulate effects of CT feedback during physiological conditions, and how much it will vary with  
401 external and internal variables, such as behavioral state. Complicating the matter further, CT feedback can increase dLGN  
402 firing not only via net depolarization, but also sustained hyperpolarization, through de-inactivation of low-threshold, T-type  
403  $\text{Ca}^{2+}$  channels<sup>57</sup> and shifts of thalamic firing to high-frequency burst-mode firing<sup>127,128</sup>. Together, instead of searching for a  
404 general rule governing effects of CT feedback, investigating to which extent excitatory and inhibitory pathways are recruited  
405 under different conditions might yield more complete answers.

## 406 References

- 407 1. Donahue, J. *et al.* DeCAF: A Deep Convolutional Activation Feature for Generic Visual Recognition. Preprint at  
408 <https://arxiv.org/abs/1310.1531> (2013).
- 409 2. Yamins, D. L. K. *et al.* Performance-optimized hierarchical models predict neural responses in higher visual cortex.  
410 *Proc. Natl. Acad. Sci. USA* **111**, 8619–8624 (2014).
- 411 3. Garg R., Carneiro G. & Reid I. Unsupervised cnn for single view depth estimation: Geometry to the rescue. In Leibe, B.,  
412 Matas, J., Sebe, N. & Welling, M. (eds.) *European Conference on Computer Vision*, 740–756 (Springer, Cham, 2016).
- 413 4. Tatarchenko M., Dosovitskiy A. & Brox T. Multi-view 3d models from single images with a convolutional network.  
414 In Leibe, B., Matas, J., Sebe, N. & Welling, M. (eds.) *European Conference on Computer Vision*, 322–337 (Springer,  
415 Cham, 2016).
- 416 5. Chen, L. C., Papandreou, G., Kokkinos, I., Murphy, K. & Yuille, A. L. DeepLab: Semantic Image Segmentation with  
417 Deep Convolutional Nets, Atrous Convolution, and Fully Connected CRFs. *IEEE Trans. on Pattern Anal. Mach. Intell.*  
418 **40**, 834–848 (2018).
- 419 6. Badrinarayanan, V., Kendall, A. & Cipolla, R. SegNet: A Deep Convolutional Encoder-Decoder Architecture for Image  
420 Segmentation. *IEEE Trans. on Pattern Anal. Mach. Intell.* **39**, 2481–2495 (2017).
- 421 7. Krizhevsky, A., Sutskever, I. & Hinton, G. E. ImageNet Classification with Deep Convolutional Neural Networks. In  
422 Pereira, F., Burges, C. J. C., Bottou, L. & Weinberger, K. Q. (eds.) *Advances in Neural Information Processing Systems*  
423 25, 1097–1105 (Curran Associates, Inc., 2012).
- 424 8. Zeiler, M. D. & Fergus, R. Visualizing and Understanding Convolutional Networks. In Fleet, D., Pajdla, T., Schiele, B.  
425 & T., T. (eds.) *European Conference on Computer Vision*, 818–833 (Springer, Cham, 2014).
- 426 9. Bashivan, P., Kar, K. & DiCarlo, J. J. Neural population control via deep image synthesis. *Science* **364**, eaav9436  
427 (2019).
- 428 10. Yamins, D. L. K. & DiCarlo, J. J. Using goal-driven deep learning models to understand sensory cortex. *Nat. Neurosci.*  
429 **19**, 356–365 (2016).
- 430 11. Walker, E. Y. *et al.* Inception loops discover what excites neurons most using deep predictive models. *Nat. Neurosci.*  
431 1–6 (2019).
- 432 12. Agam, Y. *et al.* Robust Selectivity to Two-Object Images in Human Visual Cortex. *Curr. Biol.* **20**, 872–879 (2010).
- 433 13. Hung, C. P., Kreiman, G., Poggio, T. & DiCarlo, J. J. Fast Readout of Object Identity from Macaque Inferior Temporal  
434 Cortex. *Science* **310**, 863–866 (2005).
- 435 14. Resulaj, A., Ruediger, S., Olsen, S. R. & Scanziani, M. First spikes in visual cortex enable perceptual discrimination.  
436 *eLife* **7**, e34044 (2018).
- 437 15. Harris, K. D. & Mrsic-Flogel, T. D. Cortical connectivity and sensory coding. *Nature* **503**, 51–58 (2013).
- 438 16. Sherman, S. M. & Guillery, R. W. The role of the thalamus in the flow of information to the cortex. *Philos. Trans. Royal  
439 Soc. B* **357**, 1695–708 (2002).

440 17. Heeger, D. J. Theory of cortical function. *Proc. Natl. Acad. Sci. USA* **114**, 1773–1782 (2017).

441 18. Gilbert, C. D. & Li, W. Top-down influences on visual processing. *Nat. Rev. Neurosci.* **14**, 350–63 (2013).

442 19. Hubel, D. H. & Wiesel, T. N. Integrative action in the cat's lateral geniculate body. *J. Physiol.* **155**, 385–398 (1961).

443 20. Usrey, W. M., Reppas, J. B. & Reid, R. C. Specificity and Strength of Retinogeniculate Connections. *J. Neurophysiol.* **82**, 3527–3540 (1999).

444 21. Mastronarde, D. N. Two classes of single-input X-cells in cat lateral geniculate nucleus. II. Retinal inputs and the generation of receptive-field properties. *J. Neurophysiol.* **57**, 381–413 (1987).

445 22. Rathbun, D. L., Warland, D. K. & Usrey, W. M. Spike Timing and Information Transmission at Retinogeniculate Synapses. *J. Neurosci.* **30**, 13558–13566 (2010).

446 23. Sherman, S. M. Thalamus plays a central role in ongoing cortical functioning. *Nat. Neurosci.* **16**, 533–541 (2016).

447 24. Briggs, F. & Usrey, W. M. Corticogeniculate feedback and visual processing in the primate. *J. Physiol.* **589**, 33–40 (2011).

448 25. Crandall, S. R., Cruikshank, S. J. & Connors, B. W. A Corticothalamic Switch: Controlling the Thalamus with Dynamic Synapses. *Neuron* **86**, 768–782 (2015).

449 26. Tsumoto, T., Creutzfeldt, O. D. & Legéndy, C. R. Functional organization of the corticofugal system from visual cortex to lateral geniculate nucleus in the cat. *Exp. Brain Res.* **32**, 345–364 (1978).

450 27. Angelucci, A. & Sainsbury, K. Contribution of feedforward thalamic afferents and corticogeniculate feedback to the spatial summation area of macaque V1 and LGN. *J. Comp. Neurol.* **498**, 330–351 (2006).

451 28. Ichida, J. M. & Casagrande, V. A. Organization of the feedback pathway from striate cortex (V1) to the lateral geniculate nucleus (LGN) in the owl monkey (*Aotus trivirgatus*). *J. Comp. Neurol.* **454**, 272–283 (2002).

452 29. Murphy, P. C. & Sillito, A. M. Functional morphology of the feedback pathway from area 17 of the cat visual cortex to the lateral geniculate nucleus. *J. Neurosci.* **16**, 1180–1192 (1996).

453 30. Ichida, J. M., Mavity-Hudson, J. A. & Casagrande, V. A. Distinct patterns of corticogeniculate feedback to different layers of the lateral geniculate nucleus. *Eye Brain* **2014**, 57–73 (2014).

454 31. Bonin, V., Mante, V. & Carandini, M. The Suppressive Field of Neurons in Lateral Geniculate Nucleus. *J. Neurosci.* **25**, 10844–10856 (2005).

455 32. Alitto, H. J. & Usrey, W. M. Origin and Dynamics of Extraclassical Suppression in the Lateral Geniculate Nucleus of the Macaque Monkey. *Neuron* **57**, 135–146 (2008).

456 33. McClurkin, J. W. & Marrocco, R. T. Visual cortical input alters spatial tuning in monkey lateral geniculate nucleus cells. *J. Physiol.* **348**, 135–152 (1984).

457 34. Murphy, P. C. & Sillito, A. M. Corticofugal feedback influences the generation of length tuning in the visual pathway. *Nature* **329**, 727 (1987).

458 35. Jones, H. E. *et al.* Differential feedback modulation of center and surround mechanisms in parvocellular cells in the visual thalamus. *J. Neurosci.* **32**, 15946–51 (2012).

459 36. Cudeiro, J. & Sillito, A. M. Spatial frequency tuning of orientation-discontinuity-sensitive corticofugal feedback to the cat lateral geniculate nucleus. *J. Physiol.* **490**, 481–492 (1996).

460 37. Andolina, I. M., Jones, H. E. & Sillito, A. M. Effects of cortical feedback on the spatial properties of relay cells in the lateral geniculate nucleus. *J. Neurophysiol.* **109**, 889–899 (2013).

461 38. Hasse, J. M. & Briggs, F. Corticogeniculate feedback sharpens the temporal precision and spatial resolution of visual signals in the ferret. *Proc. Natl. Acad. Sci. USA* **114**, E6222–E6230 (2017).

462 39. Webb, B. S. *et al.* Feedback from V1 and inhibition from beyond the classical receptive field modulates the responses of neurons in the primate lateral geniculate nucleus. *Vis. Neurosci.* **19**, 583–592 (2002).

482 40. Olsen, S. R., Bortone, D. S., Adesnik, H. & Scanziani, M. Gain control by layer six in cortical circuits of vision. *Nature*  
483 **483**, 47–52 (2012).

484 41. Denman, D. J. & Contreras, D. Complex Effects on In Vivo Visual Responses by Specific Projections from Mouse  
485 Cortical Layer 6 to Dorsal Lateral Geniculate Nucleus. *J. Neurosci.* **35**, 9265–9280 (2015).

486 42. Li, Y.-T., Ibrahim, L. A., Liu, B.-H., Zhang, L. I. & Tao, H. W. Linear transformation of thalamocortical input by  
487 intracortical excitation. *Nat. Neurosci.* **16**, 1324–30 (2013).

488 43. King, J. L., Lowe, M. P., Stover, K. R., Wong, A. A. & Crowder, N. A. Adaptive Processes in Thalamus and Cortex  
489 Revealed by Silencing of Primary Visual Cortex during Contrast Adaptation. *Curr. Biol.* **26**, 1295–1300 (2016).

490 44. Gong, S. *et al.* Targeting Cre Recombinase to Specific Neuron Populations with Bacterial Artificial Chromosome  
491 Constructs. *J. Neurosci.* **27**, 9817–9823 (2007).

492 45. Allen Institute for Brain Science. Technical white paper: Allen Mouse Common Coordinate Framework and Reference  
493 Atlas [http://help.brain-map.org/download/attachments/8323525/Mouse\\_Common\\_Coordinate\\_Framework.pdf?version=3&modificationDate=1508178848279&api=v2](http://help.brain-map.org/download/attachments/8323525/Mouse_Common_Coordinate_Framework.pdf?version=3&modificationDate=1508178848279&api=v2) (2017).

494 46. Wang, Q. & Burkhalter, A. Area map of mouse visual cortex. *J. Comp. Neurol.* **502**, 339–357 (2007).

495 47. Wagon, E., Mangini, N. J. & Pearlman, A. L. Retinotopic organization of striate and extrastriate visual cortex in the  
496 mouse. *J. Comp. Neurol.* **193**, 187–202 (1980).

497 48. Piscopo, D. M., El-Danaf, R. N., Huberman, A. D. & Niell, C. M. Diverse visual features encoded in mouse lateral  
498 geniculate nucleus. *J. Neurosci.* **33**, 4642–56 (2013).

499 49. Erisken, S. *et al.* Effects of Locomotion Extend throughout the Mouse Early Visual System. *Curr. Biol.* **24**, 2899–2907  
500 (2014).

501 50. Aydin, C., Couto, J. a., Giugliano, M., Farrow, K. & Bonin, V. Locomotion modulates specific functional cell types in  
502 the mouse visual thalamus. *Nat. Commun.* **9**, 4882 (2018).

503 51. Vélez-Fort, M. *et al.* The stimulus selectivity and connectivity of layer six principal cells reveals cortical microcircuits  
504 underlying visual processing. *Neuron* **83**, 1431–43 (2014).

505 52. Bortone, D. S., Olsen, S. R. & Scanziani, M. Translaminar inhibitory cells recruited by layer 6 corticothalamic neurons  
506 suppress visual cortex. *Neuron* **82**, 474–85 (2014).

507 53. Kim, J., Matney, C. J., Blankenship, A., Hestrin, S. & Brown, S. P. Layer 6 corticothalamic neurons activate a cortical  
508 output layer, layer 5a. *J. Neurosci.* **34**, 9656–64 (2014).

509 54. Frandolig, J. E. *et al.* The Synaptic Organization of Layer 6 Circuits Reveals Inhibition as a Major Output of a Neocortical  
510 Sublamina. *Cell Reports* **28**, 3131–3143.e5 (2019).

511 55. Gonchar, Y., Wang, Q. & Burkhalter, A. Multiple distinct subtypes of GABAergic neurons in mouse visual cortex  
512 identified by triple immunostaining. *Front. Neuroanat.* **1**, 3 (2007).

513 56. Jiang, X. *et al.* Principles of connectivity among morphologically defined cell types in adult neocortex. *Science* **350**,  
514 aac9462 (2015).

515 57. Sherman, S. M. Tonic and burst firing: Dual modes of thalamocortical relay. *Trends Neurosci.* **24**, 122–126 (2001).

516 58. Mitzdorf, U. Current source-density method and application in cat cerebral cortex: Investigation of evoked potentials  
517 and EEG phenomena. *Physiol. Rev.* **65**, 37–100 (1985).

518 59. Cavanaugh, J. R., Bair, W. & Movshon, J. A. Nature and interaction of signals from the receptive field center and  
519 surround in macaque V1 neurons. *J. Neurophysiol.* **88**, 2530–46 (2002).

520 60. Einevoll, G. T. & Plessner, H. E. Extended difference-of-Gaussians model incorporating cortical feedback for relay cells  
521 in the lateral geniculate nucleus of cat. *Cogn. Neurodynamics* **6**, 307–324 (2012).

522 61. Mobarhan, M. H. *et al.* Firing-rate based network modeling of the dLGN circuit: Effects of cortical feedback on  
523 spatiotemporal response properties of relay cells. *PLOS Comput. Biol.* **14**, e1006156 (2018).

524

525 62. Enroth-Cugell, C. & Pinto, L. Algebraic summation of centre and surround inputs to retinal ganglion cells of the cat.  
526 *Nature* **226**, 458–459 (1970).

527 63. Crabtree, J. W. Functional Diversity of Thalamic Reticular Subnetworks. *Front. Syst. Neurosci.* **12**, 41 (2018).

528 64. Halassa, M. M. & Acsády, L. Thalamic Inhibition: Diverse Sources, Diverse Scales. *Trends Neurosci.* **39**, 680–693  
529 (2016).

530 65. Crick, F. Function of the thalamic reticular complex: The searchlight hypothesis. *Proc. Natl. Acad. Sci. USA* **81**,  
531 4586–4590 (1984).

532 66. Sherman, S. M. & Koch, C. The control of retinogeniculate transmission in the mammalian lateral geniculate nucleus.  
533 *Exp. Brain Res.* **63**, 1–20 (1986).

534 67. McAlonan, K., Cavanaugh, J. & Wurtz, R. H. Attentional modulation of thalamic reticular neurons. *J. Neurosci.* **26**,  
535 4444–4450 (2006).

536 68. McAlonan, K., Cavanaugh, J. & Wurtz, R. H. Guarding the gateway to cortex with attention in visual thalamus. *Nature*  
537 **456**, 391–394 (2008).

538 69. Halassa, M. M. *et al.* State-Dependent Architecture of Thalamic Reticular Subnetworks. *Cell* **158**, 808–821 (2014).

539 70. Ahrens, S. *et al.* ErbB4 regulation of a thalamic reticular nucleus circuit for sensory selection. *Nat. Neurosci.* **18**,  
540 104–111 (2015).

541 71. Wimmer, R. D. *et al.* Thalamic control of sensory selection in divided attention. *Nature* **526**, 705–709 (2015).

542 72. Tervo, D. G. R. *et al.* A Designer AAV Variant Permits Efficient Retrograde Access to Projection Neurons. *Neuron* **92**,  
543 372–382 (2016).

544 73. Uhlrich, D. J., Cucchiaro, J. B., Humphrey, A. L. & Sherman, S. M. Morphology and axonal projection patterns of  
545 individual neurons in the cat perigeniculate nucleus. *J. Neurophysiol.* **65**, 1528–1541 (1991).

546 74. Funke, K. & Eysel, U. T. Inverse correlation of firing patterns of single topographically matched perigeniculate neurons  
547 and cat dorsal lateral geniculate relay cells. *Vis. Neurosci.* **15**, 711–729 (1998).

548 75. Wróbel, A. & Bekisz, M. Visual classification of X and Y perigeniculate neurons of the cat. *Exp. Brain Res.* **101**,  
549 307–313 (1994).

550 76. So, Y. T. & Shapley, R. Spatial tuning of cells in and around lateral geniculate nucleus of the cat: X and Y relay cells  
551 and perigeniculate interneurons. *J. Neurophysiol.* **45**, 107–120 (1981).

552 77. Jones, H. E. & Sillito, A. M. The Length – Response Properties of Cells in the Feline Perigeniculate Nucleus. *Eur. J.*  
553 *Neurosci.* **6**, 1199–1204 (1994).

554 78. Ruksenas, O., Fjeld, I. T. & Heggelund, P. Spatial summation and center-surround antagonism in the receptive field of  
555 single units in the dorsal lateral geniculate nucleus of cat: Comparison with retinal input. *Vis. Neurosci.* **17**, 855–870  
556 (2000).

557 79. Huang, X., Rangel, M., Briggman, K. L. & Wei, W. Neural mechanisms of contextual modulation in the retinal direction  
558 selective circuit. *Nat. Commun.* **10**, 1–15 (2019).

559 80. Jacoby, J. & Schwartz, G. W. Three Small-Receptive-Field Ganglion Cells in the Mouse Retina Are Distinctly Tuned to  
560 Size, Speed, and Object Motion. *J. Neurosci.* **37**, 610–625 (2017).

561 81. Allman, J., Miezin, F. & McGuinness, E. Stimulus specific responses from beyond the classical receptive field:  
562 Neurophysiological mechanisms for local-global comparisons in visual neurons. *Annu. Rev. Neurosci.* **8**, 407–430  
563 (1985).

564 82. Blakemore, C. & Tobin, E. A. Lateral inhibition between orientation detectors in the cat's visual cortex. *Exp. Brain. Res.*  
565 **15**, 439–440 (1972).

566 83. DeAngelis, G. C., Freeman, R. D. & Ohzawa, I. Length and width tuning of neurons in the cat's primary visual cortex. *J.*  
567 *Neurophysiol.* **71**, 347–374 (1994).

568 84. Gilbert, C. D. & Wiesel, T. N. The influence of contextual stimuli on the orientation selectivity of cells in primary visual  
569 cortex of the cat. *Vis. Res.* **30**, 1689–1701 (1990).

570 85. Knierim, J. J. & van Essen, D. C. Neuronal responses to static texture patterns in area V1 of the alert macaque monkey.  
571 *J. Neurophysiol.* **67**, 961–980 (1992).

572 86. Nelson, J. I. & Frost, B. J. Orientation-selective inhibition from beyond the classic visual receptive field. *Brain Res.* **139**,  
573 359–365 (1978).

574 87. Adesnik, H., Bruns, W., Taniguchi, H., Huang, Z. J. & Scanziani, M. A neural circuit for spatial summation in visual  
575 cortex. *Nature* **490**, 226–231 (2012).

576 88. Fisher, T. G., Alitto, H. J. & Usrey, W. M. Retinal and Nonretinal Contributions to Extraclassical Surround Suppression  
577 in the Lateral Geniculate Nucleus. *J. Neurosci.* **37**, 226–235 (2017).

578 89. Alitto, H. J. & Usrey, W. M. Surround suppression and temporal processing of visual signals. *J. Neurophysiol.* **113**,  
579 2605–2617 (2015).

580 90. Vaingankar, V., Soto Sanchez, C., Wang, X., Sommer, F. T. & Hirsch, J. A. Neurons in the thalamic reticular nucleus are  
581 selective for diverse and complex visual features. *Front. Integr. Neurosci.* **6**, 118 (2012).

582 91. Webb, B. S., Tinsley, C. J., Vincent, C. J. & Derrington, A. M. Spatial Distribution of Suppressive Signals Outside the  
583 Classical Receptive Field in Lateral Geniculate Nucleus. *J. Neurophysiol.* **94**, 1789–1797 (2005).

584 92. Nolt, M. J., Kumbhani, R. D. & Palmer, L. A. Suppression at High Spatial Frequencies in the Lateral Geniculate Nucleus  
585 of the Cat. *J. Neurophysiol.* **98**, 1167–1180 (2007).

586 93. Coen-Cagli, R., Kohn, A. & Schwartz, O. Flexible gating of contextual influences in natural vision. *Nat. Neurosci.* **18**,  
587 1648–1655 (2015).

588 94. Evangelio, M., García-Amado, M. & Clascá, F. Thalamocortical Projection Neuron and Interneuron Numbers in the  
589 Visual Thalamic Nuclei of the Adult C57BL/6 Mouse. *Front. Neuroanat.* **12**, 27 (2018).

590 95. Morgan, J. L. & Lichtman, J. W. An Individual Interneuron Participates in Many Kinds of Inhibition and Innervates  
591 Much of the Mouse Visual Thalamus. *Neuron* **106**, 468–481.e2 (2020).

592 96. Wang, X., Vaingankar, V., Sanchez, C. S., Sommer, F. T. & Hirsch, J. A. Thalamic interneurons and relay cells use  
593 complementary synaptic mechanisms for visual processing. *Nat. Neurosci.* **14**, 224–231 (2011).

594 97. Hirsch, J. A., Wang, X., Sommer, F. T. & Martinez, L. M. How Inhibitory Circuits in the Thalamus Serve Vision. *Annu.  
595 Rev. Neurosci.* **38**, 309–329 (2015).

596 98. Gorin, A., Ahn, S., Ciftcioglu, U., Sommer, F. T. & Hirsch, J. A. Receptive field structure of local interneurons in the  
597 murine dorsal lateral geniculate nucleus. Program No. 140.08. In *2019 Neuroscience Meeting Planner*, vol. Program No.  
598 140.08 (Chicago, IL, 2019).

599 99. Crandall, S. R. & Cox, C. L. Local Dendrodendritic Inhibition Regulates Fast Synaptic Transmission in Visual Thalamus.  
600 *J. Neurosci.* **32**, 2513–2522 (2012).

601 100. Gentet, L. J. & Ulrich, D. Electrophysiological characterization of synaptic connections between layer VI cortical cells  
602 and neurons of the nucleus reticularis thalami in juvenile rats. *Eur. J. Neurosci.* **19**, 625–633 (2004).

603 101. Golshani, P., Liu, X. B. & Jones, E. G. Differences in quantal amplitude reflect GluR4- subunit number at corticothalamic  
604 synapses on two populations of thalamic neurons. *Proc. Natl. Acad. Sci. USA* **98**, 4172–4177 (2001).

605 102. Kayama, Y., Shosaku, A. & Doty, R. W. Cryogenic blockade of the visual cortico-thalamic projection in the rat. *Exp.  
606 Brain Res.* **54**, 157–165 (1984).

607 103. Montero, V. M. Attentional activation of the visual thalamic reticular nucleus depends on ‘top-down’ inputs from the  
608 primary visual cortex via corticogeniculate pathways. *Brain Res.* **864**, 95–104 (2000).

609 104. Xue, J. T., Carney, T., Ramoa, A. S. & Freeman, R. D. Binocular interaction in the perigeniculate nucleus of the cat.  
610 *Exp. Brain Res.* **69**, 497–508 (1988).

611 105. Makino, H. & Komiyama, T. Learning enhances the relative impact of top-down processing in the visual cortex. *Nat.*  
612 *Neurosci.* **18**, 1116–1122 (2015).

613 106. Briggs, F. & Usrey, W. M. A Fast, Reciprocal Pathway between the Lateral Geniculate Nucleus and Visual Cortex in the  
614 Macaque Monkey. *J. Neurosci.* **27**, 5431–5436 (2007).

615 107. Stringer, C. *et al.* Spontaneous behaviors drive multidimensional, brainwide activity. *Science* **364**, 255–255 (2019).

616 108. Wiegert, J. S., Mahn, M., Prigge, M., Printz, Y. & Yizhar, O. Silencing Neurons: Tools, Applications, and Experimental  
617 Constraints. *Neuron* **95**, 504–529 (2017).

618 109. Zhao, X., Liu, M. & Cang, J. Visual Cortex Modulates the Magnitude but Not the Selectivity of Looming-Evoked  
619 Responses in the Superior Colliculus of Awake Mice. *Neuron* **84**, 202–213 (2014).

620 110. Ahmadlou, M., Tafreshiha, A. & Heimel, J. A. Visual Cortex Limits Pop-Out in the Superior Colliculus of Awake Mice.  
621 *Cereb. Cortex* **27**, 5772–5783 (2017).

622 111. Bickford, M. E., Zhou, N., Krahe, T. E., Govindaiah, G. & Guido, W. Retinal and Tectal “Driver-Like” Inputs Converge  
623 in the Shell of the Mouse Dorsal Lateral Geniculate Nucleus. *J. Neurosci.* **35**, 10523–10534 (2015).

624 112. Ahmadlou, M., Zweifel, L. S. & Heimel, J. A. Functional modulation of primary visual cortex by the superior colliculus  
625 in the mouse. *Nat. Commun.* **9**, 3895 (2018).

626 113. Mahn, M. *et al.* High-efficiency optogenetic silencing with soma-targeted anion-conducting channelrhodopsins. *Nat.*  
627 *Commun.* **9**, 4125 (2018).

628 114. Mahn, M., Prigge, M., Ron, S., Levy, R. & Yizhar, O. Biophysical constraints of optogenetic inhibition at presynaptic  
629 terminals. *Nat. Neurosci.* **19**, 554–556 (2016).

630 115. Tasic, B. *et al.* Adult mouse cortical cell taxonomy revealed by single cell transcriptomics. *Nat. Neurosci.* **19**, 335–346  
631 (2016).

632 116. Gouwens, N. W. *et al.* Classification of electrophysiological and morphological neuron types in the mouse visual cortex.  
633 *Nat. Neurosci.* **22**, 1182–1195 (2019).

634 117. Wang, W., Jones, H. E., Andolina, I. M., Salt, T. E. & Sillito, A. M. Functional alignment of feedback effects from  
635 visual cortex to thalamus. *Nat. Neurosci.* **9**, 1330–1336 (2006).

636 118. Kirchgessner, M. A., Franklin, A. D. & Callaway, E. M. Context-Dependent and Dynamic Functional Influence of  
637 Corticothalamic Pathways to First- and Higher-order Visual Thalamus. Preprint at <https://www.biorxiv.org/content/10.1101/738203v1.full> (2019).

638 119. Kwegyir-Afful, E. E. & Simons, D. J. Subthreshold Receptive Field Properties Distinguish Different Classes of  
639 Corticothalamic Neurons in the Somatosensory System. *J. Neurosci.* **29**, 964–972 (2009).

640 120. Swadlow, H. A. & Weyand, T. G. Corticogeniculate neurons, corticotectal neurons, and suspected interneurons in visual  
641 cortex of awake rabbits: Receptive-field properties, axonal properties, and effects of EEG arousal. *J. Neurophysiol.* **57**,  
642 977–1001 (1987).

643 121. Landry, P. & Dykes, R. Identification of two populations of corticothalamic neurons in cat primary somatosensory  
644 cortex. *Exp. Brain Res.* **60** (1985).

645 122. Crandall, S. R., Patrick, S. L., Cruikshank, S. J. & Connors, B. W. Infrabarrels Are Layer 6 Circuit Modules in the  
646 Barrel Cortex that Link Long-Range Inputs and Outputs. *Cell Reports* **21**, 3065–3078 (2017).

647 123. Stoelzel, C. R., Bereshpolova, Y., Alonso, J.-M. & Swadlow, H. A. Axonal Conduction Delays, Brain State, and  
648 Corticogeniculate Communication. *J. Neurosci.* **37**, 6342–6358 (2017).

649 124. Swadlow, H. A. Efferent neurons and suspected interneurons in S-1 vibrissa cortex of the awake rabbit: Receptive fields  
650 and axonal properties. *J. Neurophysiol.* **62**, 288–308 (1989).

651 125. Oberlaender, M. *et al.* Cell Type-Specific Three-Dimensional Structure of Thalamocortical Circuits in a Column of Rat  
652 Vibrissal Cortex. *Cereb. Cortex* **22**, 2375–2391 (2012).

654 126. Pauzin, F. P. & Krieger, P. A Corticothalamic Circuit for Refining Tactile Encoding. *Cell Reports* **23**, 1314–1325 (2018).

655 127. de Labra, C. *et al.* Changes in Visual Responses in the Feline dLGN: Selective Thalamic Suppression Induced by  
656 Transcranial Magnetic Stimulation of V1. *Cereb. Cortex* **17**, 1376–1385 (2007).

657 128. Spacek, M. A., Born, G., Crombie, D., Katzner, S. & Busse, L. Robust effects of cortical feedback on thalamic firing  
658 mode during naturalistic stimulation. Preprint at <https://www.biorxiv.org/content/10.1101/776237v3> (2019).

## 659 Acknowledgements

660 This research was supported by DFG BU 1808/5-1 (LB), DFG SFB870 TP19 (LB), by an add-on fellowship of the Joachim  
661 Herz Stiftung (GB), by DFG SFB 870 Z04 (M. Götz), and by the Viral Vector Facility of the LMU. We thank A. Wal for  
662 recording some of the data in **Figure 2**, and I. Mühlhahn for CsCl DNA preparation. We are grateful to M. Sotgia for lab  
663 management and support with animal handling and histology, S. Schörnich for IT support, and B. Grothe for providing excellent  
664 research infrastructure.

## 665 Author contributions statement

666 Conceptualization, L.B., S.E., G.B., F.A.S.; Methodology, M.H.M., G.E.; Software, G.B., S.E., F.A.S., M.A.S., M.H.M., L.B.;  
667 Formal Analysis, G.B., S.E., F.A.S., L.B.; Investigation, G.B., S.E., A.K., F.A.S., M.A.S.; Resources, C.L.L.; Data Curation,  
668 M.A.S., G.B., S.E., L.B., F.A.S.; Writing – Original Draft, G.B., S.E., F.A.S., L.B.; Writing – Review & Editing, all authors;  
669 Visualization, G.B., S.E., F.A.S., L.B.; Supervision, L.B.; Project Administration, L.B.; Funding Acquisition, L.B., G.B.

## 670 Competing interests

671 The authors declare no competing interests

## 672 Additional information

### 673 Methods

674 All procedures complied with the European Communities Council Directive 2010/63/EC and the German Law for Protection of  
675 Animals, and were approved by local authorities, following appropriate ethics review.

676 Experiments were performed in 36 adult mice of three strains (C57BL/6J:  $n = 3$ , mean age = 14.2 weeks; B6;129P2-  
677 Pvalb<sup>tm1(cre)Arbr</sup>/J:  $n = 18$ , mean age = 23.8 weeks both Jackson Laboratory; B6.FVB(Cg)-Tg(Ntsr1-cre)GN220Gsat/Mmcd:  
678  $n = 15$ , mean age = 22.8 weeks, MMRRC) of either sex.

### 679 Surgical procedures for headpost implantation, virus injection and craniotomy

680 The majority of mice were treated according to licence ROB-55.2-2532.Vet\_02-17-40: Thirty minutes prior to surgery,  
681 an analgesic (Metamizole, 200 mg/kg, sc, MSD Animal Health, Brussels, Belgium) was administered. Anesthesia was  
682 induced by placing the mice in an induction chamber and exposing them to isoflurane (5% in oxygen, CP-Pharma, Burgdorf,  
683 Germany). Animals were then fixated in a stereotaxic frame (Drill & Microinjection Robot, Neurostar, Tuebingen, Germany),  
684 and isoflurane level was adjusted (0.5%–2% in oxygen) to maintain an appropriate level of anesthesia, evaluated by the  
685 absence of the pedal reflex. During the procedure, the eyes were protected with an ointment (Bepanthen, Bayer, Leverkusen,  
686 Germany) and the animal's body temperature was maintained at 37° C by means of a closed loop temperature control system  
687 (ATC 1000, WPI Germany, Berlin, Germany). An additional analgesic was delivered (Buprenorphine, 0.1 mg/kg, sc, Bayer,  
688 Leverkusen, Germany). After the animal's head had been shaved, the skin was thoroughly disinfected with iodine solution  
689 (Braun, Melsungen, Germany), a local analgesic (Lidocaine hydrochloride, 7 mg/kg, sc, bela-pharm, Vechta, Germany) was  
690 injected under the scalp, and a small incision along the midline was cut. Part of the skin covering the skull was removed, and  
691 tissue residues were cleaned by administration of a drop of H<sub>2</sub>O<sub>2</sub> (3%, AppliChem, Darmstadt, Germany). The animal's head  
692 was adjusted to a skull-flat configuration using four landmarks (bregma, lambda, and two points 2 mm to the right and to the  
693 left of the midline respectively). OptiBond FL primer and adhesive (Kerr dental, Rastatt, Germany) were applied to the exposed  
694 skull, except for locations of the future craniotomy and a location approximately 1.5 mm anterior and 1 mm to the right of

695 bregma, were a miniature reference screw (00-96 X 1/16 stainless steel, Bilaney) soldered to a custom-made connector pin was  
696 implanted.

697 For cre-dependent expression of ChR2 in PV-Cre and Ntsr1-Cre mice, 2  $\mu$ L of an adeno-associated virus (pAAV-EF1a-  
698 double floxed-hChR2(H134R)-EYFP-WPRE-HGHpA (Addgene, #20298), with different serotypes and titers  $\geq 7 \times 10^{12}$  vg/mL)  
699 was mixed with 0.3  $\mu$ L fast green (Sigma-Aldrich, St. Louis, USA). A small craniotomy was performed over V1 ((AP: -2.8 mm,  
700 ML: -2.5 mm); (AP: -2.8 mm, ML: -2.3 mm); (AP: -3.08 mm, ML: -2.5 mm) or (AP: -3.28, ML: -2.4 mm)) to enable  
701 injection of the prepared mixture. In PV-cre mice, a total of  $\sim 0.2 - 0.5 \mu$ L of the mixture was injected in multiple depths  
702 between 1000  $\mu$ m and stopping at 100  $\mu$ m below the pial surface. In Ntsr1-Cre mice used for global L6 photostimulation  
703 (**Figure S2**),  $< 0.5 \mu$ L was injected at depths between 800  $\mu$ m and 1000  $\mu$ m, approximately targeting L6. In 3 Ntsr1-Cre  
704 mice, used for mapping of L6CT feedback (**Figure 1**), only  $\sim 0.05 \mu$ L was injected at a depth of  $\sim 900 \mu$ m. For retrograde  
705 labelling of visTRN cells, 0.5  $\mu$ L of the adeno-associated viral vector rAAV2/retro CMV-GFP (titer:  $1.61 \times 10^{15}$  GC/ml) was  
706 mixed with 1.5  $\mu$ L PBS and 0.3  $\mu$ L fast green. In 3 mice, a small craniotomy was performed above dLGN (AP: -2.3 mm,  
707 ML: -2.3 mm) and 0.4  $\mu$ L of the prepared mixture was injected at a depth of -2.8 mm. Injections were carried out using a  
708 Hamilton syringe (SYR 10  $\mu$ L 1701 RN no NDL, Hamilton, Bonaduz, Switzerland) equipped with a glass pipette.

709 Above the posterior part of the skull and on top of the primer/adhesive, a custom-made lightweight stainless steel head  
710 bar with a cutout for the future craniotomy was attached with dental cement (Ivoclar Vivadent, Ellwangen, Germany). At the  
711 end of the procedure, the cutout was covered with the silicone elastomer sealant Kwik-Cast (WPI Germany, Berlin, Germany)  
712 and an antibiotic ointment (Imax, Merz Pharmaceuticals, Frankfurt, Germany) was applied to the borders of the wound. The  
713 long-term analgesic (Meloxicam, 2 mg/kg, sc, Böhringer Ingelheim, Ingelheim, Germany) was injected immediately following  
714 the surgery and continued to be administered in 24 h intervals for 3 consecutive days. For a period of 5 days post-surgery, the  
715 animal's health status was assessed with a score sheet.

716 A smaller number of mice ( $n = 15$ ) were treated according to licence CIN 4/12, in which general surgical procedures  
717 were identical with the following exceptions: After induction of anesthesia, mice were additionally injected with atropine  
718 (Atropine sulfate, 0.3 mg/kg, sc, Braun, Melsungen, Germany). The headpost consisted of a small S-shaped piece of aluminum,  
719 which was cemented to the skull between lambda and bregma and to the right of the midline. Virus was injected with either  
720 a Picospritzer (Parker Hannifin, Hollis, USA) or a Nanoject (Drummond Scientific, Broomall, USA). Posterior to the head  
721 post, over the cerebellum, two miniature screws serving as ground and reference were implanted. A well of dental cement  
722 was formed over the target recording and stimulation sites and filled with Kwik-Cast. At the end of the procedure, antibiotics  
723 (Baytril, 5 mg/kg, sc, Bayer, Leverkusen, Germany) and a long-term analgesic (Carprofen, 5 mg/kg, sc, Rimadyl, Zoetis, Berlin,  
724 Germany) were administered and continued to be given for 3 days post-surgery.

725 To compare visTRN RFs to dLGN RFs (**Figure 4d**), we included dLGN recordings from 16 mice (8 PV-Cre and 8 Ntsr1-Cre  
726 mice). In 6 of these Ntsr1-Cre mice, V1 was injected with a virus irrelevant for the purpose of our investigation (AAV-DJ-Ef1a-  
727 DIO SwiChR++-EYFP,  $n = 2$ ; pAAV\_hSyn1-SIO-stGtACR2-FusionRed (Addgene #105677),  $n = 4$ ).

728 Gradual habituation of the animal to the experimental condition started after at least 7 days of recovery. The habituation  
729 phase consisted of 3 days of handling followed by 4 days during which the experimental procedure was simulated. In mice  
730 prepared for photostimulation experiments, neural recordings did not start sooner than 3 weeks post injection to give enough  
731 time for virus expression. One day before the first recording session, mice were anesthetized in the same way as for the initial  
732 surgery. For V1 and dLGN recordings, a craniotomy (ca.  $1.5 \text{ mm}^2$ ) was performed above V1 and dLGN (AP: -2 or -2.5 mm,  
733 ML: -2 mm). For TRN recordings, two smaller craniotomies (ca.  $1 \text{ mm}^2$ ) were performed over V1 and TRN respectively (V1:  
734 AP: -2.8 mm, ML: -2.5 mm; TRN: AP: -1.25 mm, ML: -2.15 mm; or AP: -1.25 mm, ML: -2.2 mm; or AP: -1 mm,  
735 ML: -2 mm). At the end of the procedure, the craniotomy was re-sealed with Kwik-Cast. To avoid residual drug effects  
736 during the recordings, the long-term analgesic Metacam was injected only once at the end of the surgery, unless the mouse  
737 showed any sign of distress. Experiments started the day after craniotomy, carried out daily and continued for as long as the  
738 electrophysiological signal remained of high quality.

### 739 **rAAV2/retro production**

740 High-titer preparations of rAAV2/retro were produced based on the protocol of Zolotukhin and colleagues<sup>S1</sup> with minor  
741 modifications. In brief, HEK 293T cells (ATCC CRL-3216) were transfected with the CaPO4 precipitation method, where  
742 the plasmids rAAV2-retro (Addgene #81070)<sup>72</sup>, Ad helper (Cell Biolabs, Cat.N: gb AF369965.1) and pAAV-CMV-GFP

743 (Cell Biolabs, Cat.N: AAV-400) were applied in an equimolar ratio (all plasmids were CsCl gradient purified). After 96 h,  
744 the cell pellet was harvested with the AAV release solution, 50 U/ml benzonase was added, and the solution was incubated  
745 for 2 h at 37° C. Cells were frozen and thawed in liquid nitrogen to allow rAAV release. Purification of the rAAV vector  
746 was done with iodixanol densities gradient (consisting of 15, 25, 40 and 56% iodixanol), followed by gradient spinning at  
747 50.000 rpm for 2 h 17 min at 22° C in a Ti70 rotor (Beckman, Fullerton, CA, USA). rAAV was collected at 40% iodixanol with  
748 a 5 ml syringe. Virus was dialyzed (Slide-A-Lyzer 10.000 MWCO 5ml) in buffer A overnight to remove iodixanol. Anion  
749 exchange chromatography column HiTrap Q FF sepharose column and Superloop were connected with the ÄKTAprime plus  
750 chromatography system to collect the eluted fraction. To measure rAAV concentration, the eluted fraction was spun and washed  
751 once in PBS-MK Pluronic-F68 buffer with a Millipore 30K MWCO 6 ml filter unit. rAAVs were stored in a glass vial tube at  
752 4° C. rAAVs were titered by SYBR Green qPCR with GFP primer<sup>S2</sup>. Usual titer was  $5 \times 10^{13}$  to  $5 \times 10^{15}$  GC/mL.

### 753 **Electrophysiological recordings and optogenetic manipulations**

754 Recording sessions were carried out in a secluded chamber that allowed to run experiments in the absence of any ambient light  
755 source. Animals were head-fixed and positioned on an air-cushioned Styrofoam ball that enabled the mouse to freely move.  
756 Ball movements were recorded at 90 Hz by two optical computer mice connected to a microcontroller (Arduino Duemilanove).  
757 Eye position and pupil size were recorded under infrared light illumination by a camera (Guppy AVT camera; frame rate 50 Hz,  
758 Allied Vision, Exton, USA) interfaced with a zoom lense (Navitar Zoom 6000, Rochester, USA). Extracellular activity was  
759 sampled at 30 kHz (Blackrock Microsystems, Salt Lake City, USA). At the beginning of each recording session, the silicone  
760 plug covering the craniotomy was removed and a silicon probe (A1x32Edge-5mm-20-177-A32, A1x32-5mm-25-177, A1x16-  
761 3mm-50-177-A16, A1x64-Poly2-6mm-23s-160, NeuroNexus, Ann Arbor, USA; H3, Cambridge NeuroTech, Cambridge, UK)  
762 was lowered above the target site by a micromanipulator (MP-225, Sutter Instrument, Novato, CA, USA) to the appropriate  
763 depth (mean recording depth in  $\mu\text{m}$ : V1: 1040; dLGN: 3074; visTRN: 3394), until we encountered vigorous responses to  
764 visual stimuli. For recordings from dLGN and TRN, we judged the correct position of the electrode based on *post mortem*  
765 histological reconstruction of the electrode track, for which we stained the electrode with a lipophilic fluorescent tracer (DiI,  
766 DiD, Invitrogen, Carlsbad, USA) on one of the final recording sessions. For recordings from dLGN, where physiological  
767 properties are well known<sup>48, S3</sup>, additional indicators were the characteristic progression of RFs from upper to lower visual field  
768 along the electrode shank, the neurons' preference for drifting gratings of high temporal frequency, and the manifestation of  
769 this frequency in the response pattern of the cells (strong F1 response).

770 To photostimulate PV+ inhibitory interneurons or L6CT cells, we interfaced an optic fiber (910  $\mu\text{m}$  diameter, Thorlabs,  
771 Newton, USA) with a blue light-emitting diode (LED) (center wavelength 470 nm, M470F1, Thorlabs, Newton, USA; or center  
772 wavelength 465 nm, LEDC2\_465/635\_SMA, Doric lenses, Quebec, Canada). The tip of the fiber was placed less than 1 mm  
773 above the exposed surface of V1 using a manual micromanipulator. The tip of the head bar holder was surrounded with black  
774 metal foil that prevented the light from reaching the animal's eyes. For each mouse, the first recording session was conducted in  
775 V1 to verify that the photostimulation was effective. Only if light exposure reliably triggered suppression of V1 for PV-Cre  
776 mice or activation of L6 for Ntsr1-Cre mice, the animal was used for subsequent recording from dLGN or TRN. To elicit  
777 reliable effects during each recording session, we adjusted the light intensity of the LED on a daily basis (median intensity:  
778 0.04 mW/mm<sup>2</sup> as measured at the tip of the optic fiber).

### 779 **Visual stimulation**

780 We used a gamma-corrected liquid crystal display (LCD) monitor (Samsung Sync-Master 2233RZ; mean luminance 50 cd/m<sup>2</sup>)  
781 positioned at 25 cm distance from the animal's right eye and custom written software (EXPO, <https://sites.google.com/a/nyu.edu/expo/home>) to present visual stimuli.

### 783 **RF mapping and identification of cortical layers**

784 We mapped RFs with a sparse noise stimulus, which consisted of non-overlapping black and white squares with a side length of  
785 4 or 5 deg that were arranged on a grid spanning between 40 and 60 deg on each side. Stimulus presentation time differed  
786 between experiments and ranged between 0.08 and 0.20 s. Whenever possible, subsequent stimuli were presented at RF  
787 locations based on multiunit activity extracted from the ongoing recordings by applying a threshold of 4.5 to 6.5 SD to the  
788 high-pass filtered signals.

789 To determine the V1 laminar location of the recording sites, we presented full-field, contrast-reversing checkerboards at  
790 100% contrast, with a check size of 25 deg and a temporal frequency of 0.5 cyc/s.

791 **Tuning experiments**

792 Drifting gratings adapted in their temporal (0.20 – 15.00 cyc/s) and spatial frequencies (0.01 – 0.08 cyc/deg) to the preferences  
793 of neurons at the recording site, were used to determine selectivity for orientation, contrast and size. Contrast was set to 1 for  
794 all gratings except those in contrast tuning experiments. In all tuning experiments, we assessed spontaneous firing rate by  
795 including trials, in which only the mean luminance gray screen was presented. Effects of photostimulation were computed  
796 using photostimulation windows and corresponding windows in control conditions during stimulus presentation.

797 To verify effectiveness of photostimulation, we performed the first recording session for each animal in area V1, where we  
798 used drifting sinusoidal gratings to measure tuning for various stimulus properties, with photostimulation trials interleaved in  
799 pseudorandom order. For the analysis of V1 suppression by photoactivating PV+ inhibitory interneurons (Figure 2a-c), we  
800 pooled data from direction tuning experiments ( $n = 11$ ), size tuning experiments ( $n = 19$ ), and contrast tuning experiments  
801 ( $n = 10$ ). For direction tuning experiments, grating direction varied either in step sizes of 30 deg or 45 deg. Gratings were either  
802 presented for 0.75 s with photostimulation starting with stimulus onset and lasting for 0.85 s, or for 1.5 s with photostimulation  
803 starting with stimulus onset and lasting for 1.6 s, or for 2 s with photostimulation starting 0.85 s after stimulus onset and lasting  
804 for 0.25 s. For size tuning experiments, gratings ranged in diameter between 0 and 67 deg (in 11 or 15 steps). Stimuli were  
805 presented for either 1.5 s with photostimulation starting with stimulus onset and lasting for 1.6 s, or 0.75 s with photostimulation  
806 starting 0.21 s after stimulus onset and lasting for 0.25 s. Lastly, for contrast tuning experiments, contrast varied in 13 steps  
807 between 0 and 1. Stimuli were presented for 2 s, and photostimulation started 0.85 s after stimulus onset and lasted for 0.25 s.

808 For the analysis of L6CT activation effects in V1 during photostimulation of Ntsr1+ neurons (Figure S2a-c), we again  
809 pooled data from direction ( $n = 11$ ), size ( $n = 11$ ), and contrast ( $n = 6$ ) tuning experiments. For direction tuning experiments,  
810 grating direction varied in step sizes of 30 deg. Gratings were presented either for 0.75 s with photostimulation starting 0.1 s  
811 before stimulus onset and lasting for 0.85 s or for 0.75 s with photostimulation starting 0.15 s after stimulus onset and lasting  
812 for 0.25 s. For size tuning experiments, grating diameter varied between 0 and 67 deg in 13 steps. Gratings were presented for  
813 0.75 s with photostimulation starting 0.10 s before stimulus onset and lasting for 0.85 s, or for 0.75 s with photostimulation  
814 starting 0.15 s after stimulus onset and lasting for 0.25 s. Finally, for contrast tuning experiments, contrast levels ranged  
815 between 0 and 1 in 13 steps. Gratings were presented for 0.75 s with photostimulation starting 0.1 s before stimulus onset and  
816 lasting for 0.85 s.

817 To assess functional specificity of CT feedback (Figure 1g-k), we relied on activity measured during orientation tuning  
818 experiments. Sinusoidal gratings drifting in different directions (0 -330 deg, step size = 30 deg) were presented with and without  
819 photostimulation in pseudorandom order. During most experiments ( $n = 14$ ), stimuli were presented for 0.75 s, photostimulation  
820 started 0.1 s before stimulus onset and lasted for 0.85 s. In a small fraction of experiments ( $n = 4$ ), stimuli were presented for  
821 1 s, photostimulation started 0.15 s before stimulus onset and lasted for 1.35 s.

822 To assess effects of V1 suppression on spatial integration in dLGN (Figure 2h-l), we used drifting gratings with stimulus  
823 diameter ranging between 0 and 67 deg (in 11 or 15 steps). Gratings were presented for 0.75 s with photostimulation starting  
824 with stimulus onset and lasting for 0.85 s, or for 1.5 s and photoactivation starting with stimulus onset and lasting for 1.6 s, or  
825 for 0.75 s with photostimulation starting 0.25 s after stimulus onset and lasting for 0.25 s. To probe size tuning in visTRN  
826 ( $n = 69$  experiments, Figure 4e-h), we used sinusoidal or square-wave drifting gratings with diameters ranging between 0 and  
827 67 deg (in 11 or 15 steps). Stimuli were presented for 0.75 s. In a subset of experiments with paired photoactivation of PV+  
828 neurons in V1 ( $n = 31$ , Figure 5), photoactivation started with stimulus onset and lasted for 0.85 s.

829 **Spontaneous activity**

830 To probe the effect of suppressing CT feedback on spontaneous activity in dLGN, we photoactivated PV+ neurons in V1 in the  
831 absence of visual stimulation ( $n = 28$  experiments). Photostimulation periods differed between experiments, and ranged from  
832 0.17 s to 1 s.

833 **Histology**

834 To verify recording site and virus expression, we performed histological analyses. For experiments under licence ROB-  
835 55.2-2532.Vet\_02-17-40, after the final recording session, mice were first administered with an analgesic (Metamizole) and

836 after 30 min anesthetized with isoflurane and injected (ip) with a mix of Medetomidin (Domitor, 0.5 mg/kg, Vetoquinol,  
837 Ismaning, Germany), Midazolam (Climasol, 5 mg/kg, Ratiopharm, Ulm, Germany) and Fentanyl (Fentadol, 0.05 mg/kg,  
838 Dechra Veterinary Products Deutschland, Aulendorf, Germany). Under deep anesthesia, mice were then perfused with 4%  
839 paraformaldehyde (PFA) phosphate buffered saline (PBS) solution. Brains were removed, postfixed in PFA for 24 h, and then  
840 rinsed with and stored in PBS at 4° C. Coronal brain slices (40  $\mu$ m) were cut using a vibratome (Leica VT1200 S, Leica,  
841 Wetzlar, Germany), stained with DAPI solution before (DAPI, Thermo Fisher Scientific, Waltham, Massachusetts, USA;  
842 Vectashield H-1000, Vector Laboratories, Burlingame, USA) or after mounting them on glass slides (Vectashield DAPI), and  
843 coverslipped. A scanning fluorescent microscope (BX61 Systems Microscope, Olympus, Tokyo, Japan) was used to inspect  
844 slices for the presence of yellow fluorescent protein (eYFP), green fluorescent protein (GFP), DiI, and DiD. For experiments  
845 under licence CIN 4/12, general histological procedures were identical with the following exceptions: Mice were injected with  
846 sodium pentobarbital (Narcoren, 200 mg/kg, ip, Böhringer Ingelheim, Ingelheim, Germany) before the perfusion. Coronal brain  
847 slices (50  $\mu$ m) were obtained by using a vibratome (Microm HM 650 V, Thermo Fisher Scientific, Waltham, Massachusetts,  
848 USA) and inspected with a Zeiss Imager.Z1m fluorescent microscope (Zeiss, Oberkochen, Germany).

849 For atlas registration and 3D reconstruction, whole brain images were obtained. Images were processed off-line using  
850 FIJI<sup>S4, S5</sup>.

### 851 **3D reconstruction of expression volumes**

852 For 3D reconstruction and volumetric quantification of expression volumes in L6 and dLGN, brain slice images had to  
853 be annotated and mapped to stereotaxic coordinates for each pixel. To this end, brain slice images were registered to the  
854 Allen Common Coordinate Framework (CCF)<sup>45</sup>, using the allenCCF tools software package (<https://github.com/cortex-lab/allenCCF>)<sup>S6</sup>. In brief, for each brain slice, best corresponding atlas sections were chosen manually. To find  
855 the optimal transform between atlas coordinates and image pixels, reference points between the atlas section and brain slice  
856 image were manually set at unambiguous and salient features of the brain, including structures of the hippocampus, ventricle  
857 borders along the midline, habenular nuclei, the midline crossing of the corpus callosum, the indent between the ventral end  
858 of the hippocampal formation and the hypothalamus, the meeting point between the medial amygdala and the hypothalamus  
859 and high curvature turning points of the brain outline. After successful registration, points set manually along the outline  
860 of the expression zones were exported in stereotaxic coordinates. Repeating these steps for the brain slices containing the  
861 target regions yielded point clouds in 3D space, circumscribing the expression zones in cortex and thalamus. We computed  
862 the convex hull of each point cloud as a geometric description of the expression volume. We chose the convex hull, because  
863 it is unambiguously defined for any set of points and does not require prior assumptions about the shape of the volume. To  
864 constrain the expression volume with respect to the potentially non-convex structure of the brain area it occupies, we computed  
865 the intersection between the convex hull and the 3D model of the brain area of interest (V1 L6 or dLGN). This process yielded  
866 a 3D model of that part of the expression zone, which was embedded in the brain area of interest. The intersection operations  
867 and computations of volumes on the 3D models were performed with specialized geometry processing software for Python  
868 (PyMesh, <https://github.com/PyMesh>).

### 870 **Locomotion**

871 For recordings under licence ROB-55.2-2532.Vet\_02-17-40 (Figures 4–5), we computed run speed by using the Euclidean  
872 norm of three perpendicular components of ball velocity (roll, pitch, and yaw)<sup>S7</sup> and smoothed traces with a Gaussian filter  
873 ( $\sigma = 0.2$  s). For all analyses of electrophysiological data except for RF mapping with the sparse noise stimulus, we only  
874 considered trials in which the animal was sitting. Sitting trials were defined as trials in which the speed of the animal remained  
875 below 0.25 cm/s for at least 50% of the time. For recordings performed under licence CIN 4/12 (Figures 1k–2, and associated  
876 supplemental figures), the Gaussian filter differed slightly ( $\sigma = 0.15$  s), and hence sitting trials where defined by a run speed  
877 below 1 cm/s for 80% of the analyzed time window.

### 878 **Spike sorting**

879 Data in Figures 1k, 4, and 5 (and associated supplemental figures), were filtered using a 4<sup>th</sup> order Butterworth high-pass  
880 non-causal filter with a low frequency cutoff of 300 Hz and removed any saturation in the signal before clustering responses  
881 with the Matlab-based, automated spike sorting software Kilosort<sup>S8</sup>. The resulting clusters were imported to the Python  
882 toolbox Spyke<sup>S9</sup> for manual refinement of clusters. Spyke allows to select time ranges and channels around clustered spikes for

883 realignment and for representation in 3D space using dimensionality reduction (multichannel PCA, ICA, and/or spike time).  
884 In 3D, clusters were further separated by a gradient-ascent based clustering algorithm (GAC)<sup>S10</sup>. Using exhaustive pairwise  
885 comparison of similar clusters, we merged potentially overclustered units. Only clusters whose autocorrelogram displayed a  
886 clear refractory period and whose mean voltage trace showed a characteristic spike waveshape were considered for subsequent  
887 analyses.

888 For data in Figures 1k–2 (and associated supplemental figures), single neurons in our linear array recordings were isolated  
889 by grouping neighboring channels into 5 equally sized “virtual octrodes” (8 channels per group with 2 channel overlap for 32  
890 channel probes). Using an automatic spike detection threshold<sup>S11</sup> multiplied by a factor of 1.5, spikes were extracted from the  
891 high-pass filtered continuous signal for each group separately. The first 3 principal components of each channel were used for  
892 semi-automatic isolation of single neurons with KlustaKwik<sup>S12</sup>; the resulting clusters were manually refined with Klusters<sup>S13</sup>.  
893 Only clusters whose autocorrelogram displayed a clear refractory period and whose mean voltage trace showed a characteristic  
894 spike waveshape were further considered. In order to avoid duplication of neurons extracted from linear probe recordings, we  
895 computed cross-correlograms (CCHs, 1 ms bins) between pairs of neurons from neighboring groups. Pairs for which the CCH’s  
896 zero-bin was 3× larger than the mean of non-zero-bins were considered to be in conflict, and only one was kept.

897 Extracted single units were assigned to the electrode contact with the largest waveform.

### 898 **Analysis of multiunit activity**

899 To obtain robust estimates of RFs at the V1 injection site, we used the envelope of multiunit activity (MUAe), which reflects  
900 the number and amplitude of spikes close to the electrode and resembles thresholded multiunit data and average single-unit  
901 activity<sup>S14,S15</sup>. For calculating the MUAe, the median-subtracted, high-pass filtered signals were full-wave rectified, before  
902 low-pass filtering (200 Hz) and down-sampling to 2000 Hz<sup>S14–S16</sup>.

### 903 **Assignment of units to V1 layers**

904 We assigned units to V1 layers by current source density (CSD) analyses<sup>58</sup>. The local field potential (LFP) was computed  
905 by downsampling the wideband signal to 1250 Hz. For V1 recordings, the LFP was triggered to contrast reversals of the  
906 checkerboard stimulus. The CSD was computed by taking the second spatial derivative of the LFP<sup>58</sup> and spatially smoothing  
907 with a triangular kernel<sup>S17</sup>. The contact closest to the earliest CSD polarity inversion was assigned to the base of layer 4<sup>S18</sup>.  
908 The remaining contacts were assigned to putative supragranular, granular and infragranular layers based on a cortical thickness  
909 of 1 mm and anatomical measurements of relative layer thickness in mouse V1<sup>S19</sup>.

### 910 **Data analysis**

911 All further analyses were conducted with custom-written code in Matlab or Python, using the DataJoint framework<sup>S20</sup>.

912 We calculated mean percent change as

$$\Delta\%(x) = (2^{\frac{\sum_{k=1}^n \log_2(\frac{x_{\text{supp},k}}{x_{\text{cont},k}})}{n}} - 1) * 100, \quad (1)$$

913 where  $x_{\text{supp}}$  and  $x_{\text{cont}}$  represent the measured variable under the control condition and under the photostimulation condition  
914 respectively, and  $n$  is the number of observations.

### 915 **Descriptive modelling of tuning curves**

916 To characterize neural selectivity, we fit descriptive models and determined goodness of fit by  $R^2 = 1 - (SSE/SST)$ , where  
917  $SSE = \sum(y - \hat{y})^2$  and  $SST = \sum(y - \bar{y})^2$ .

### 918 **Receptive field fitting**

Receptive field maps obtained in sparse noise experiments were fit by a 2D-Gaussian<sup>S21</sup>.

$$f(x, y) = \frac{A}{2\pi ab} \exp\left(-\frac{x'^2}{2a^2} - \frac{y'^2}{2b^2}\right) + c \quad (2)$$

919 where  $A$  is the maximum amplitude,  $a$  and  $b$  are half-axes of the ellipse, and  $x'$  and  $y'$  are the transformations of the stimulus  
920 coordinates  $x$  and  $y$ , considering the angle  $\theta$  and the coordinates of the center  $(xc, yc)$  of the ellipse, and  $c$  is an offset. RF area

921 (Figure 4d-h and Figure 5) was calculated at 1 sigma.

922 In analyses where we relied on MUAE activity (Figure 1i-k), the RF maps were based on MUAE activity between 50 and  
 923 100 ms after stimulus onset (both black and white squares). For the comparison of classical RF sizes in dLGN and visTRN  
 924 (Figure 4c,d), the RF maps were based on single unit responses to both bright and dark stimuli. Before fitting the 2D-Gaussian,  
 925 mean responses were normalized by first subtracting the minimum response and then dividing by the range.

926 Responses in direction tuning experiments (Figure 1k and Figure 2b) were fit with a sum of two Gaussians with peaks  
 927 180 deg apart, which could have different amplitudes but equal width and a constant baseline<sup>S22</sup>:

$$R(\theta) = R_0 + R_p e^{-\frac{(\theta-\theta_p)^2}{2\sigma^2}} + R_n e^{-\frac{(\theta-\theta_p+180)^2}{2\sigma^2}}, \quad (3)$$

928 where  $\theta$  is stimulus direction (0–360 deg). The function has five parameters: preferred direction  $\theta_p$ , tuning width  $\sigma$ ,  
 929 baseline response  $R_0$ , response at the preferred direction  $R_p$ , and response at the null direction  $R_n$ .

### 930 **Size tuning**

To analyze size tuning in dLGN, we fit responses to drifting gratings of different sizes with a ratio of Gaussians model<sup>59</sup>, where a center Gaussian is normalized by a Gaussian representing the surround, each having their independent amplitude ( $k$ ) and width ( $w$ ):

$$R(x) = \frac{k_c L_c(x)}{1 + k_s L_s(x)} \quad (4)$$

$$L_c(x) = \left( \frac{2}{\sqrt{\pi}} \int_0^x e^{-(y/w_c)^2} dy \right)^2 \quad (5)$$

$$L_s(x) = \left( \frac{2}{\sqrt{\pi}} \int_0^x e^{-(y/w_s)^2} dy \right)^2 \quad (6)$$

931 We always constrained  $w_c < w_s$ .

To analyze spatial integration in visTRN (Figure 4e-h and Figure 5), we included an offset ( $b$ ) and allowed for rectification of the size tuning curve, to better capture spatial integration in neurons whose firing rates were substantially reduced during V1 suppression:

$$R(x) = \max(0, \frac{k_c L_c(x)}{1 + k_s L_s(x)} + b) \quad (7)$$

932 We subtracted the modelled response to stimulus size 0 deg from the resulting curve and quantified suppression strength  
 933 with a suppression index:  $SI = (R_{\text{opt}} - R_{\text{supp}})/R_{\text{opt}}$ , where  $R_{\text{opt}}$  is the peak response and  $R_{\text{supp}}$  is the response to the largest  
 934 stimulus diameter (75 deg). The peak response was defined as the response to the stimulus diameter for which a 1 deg increment  
 935 in size failed to increase the modelled firing rate by 0.05%.

### 936 **Quantification of RFs for functional mapping of CT feedback**

937 To quantify average RF location at the V1 injection site Figure 1i, we computed for each channel a RF map based on MUAE  
 938 activity. Channels with poor fits of the 2D Gaussians ( $R^2 < 0.4$ ) were not considered for further analyses. Average V1 RF  
 939 location was obtained by averaging the center positions over all 2D Gaussians. To quantify the retinotopic distance of dLGN  
 940 neurons with respect to the V1 injection site, we computed the euclidean distance between their channels' MUAE RF center  
 941 and the retinotopic location of the V1 injection site.

### 942 **Spatial profile of CT feedback**

943 To quantify the spatial profile of CT feedback (Figure 1k), we used direction tuning experiments. We focused on visually  
 944 driven units, defined by their evoked firing rate differing from spontaneous activity by at least  $3.29 \times$  the standard error of the

945 mean (s.e.m.) for at least one direction, with average firing rates  $\geq 0.15$  sp/s. We computed for each unit and direction the log2  
946 ratio of firing rates with photoactivation and in the corresponding control condition, before averaging across directions.

947 To assess the spatial profile of CT feedback effects in dLGN, we grouped neurons according to their retinotopic distance to  
948 the V1 injection zone into overlapping bins (15 deg width, 3.3 deg spacing; average number of units per bin: 66; minimum  
949 number of units per bin: 32, except for last bin: 7 units). We estimated the 95% CI of the mean effect per bin by resampling  
950 with replacement (1000 iterations). To test for spatial regions with a significant CT feedback effect, we used a cluster-based  
951 permutation test<sup>S23</sup>. We grouped all neighbouring bins with mean log2 ratios significantly different from 0 (0 not within  
952 95% CI) and the same sign into clusters, and computed the sum of absolute mean log2 ratios within those clusters. We then  
953 considered the maximum absolute cluster sum value as the test statistic. These analysis steps were then repeated over 10000  
954 iterations with randomly permuted distance values across all neurons. The p-value was the proportion of random permutations  
955 which yielded a cluster sum larger than the one from our original data set.

956 Next, we classified single neurons into significantly enhanced, suppressed or not modulated depending on whether their  
957 average log2 ratio was above, below or within the 95% interval of the sampling distribution obtained from permuting the  
958 photoactivation labels of trials within directions and recomputing the average log2 ratio across directions (10000 iterations). To  
959 test whether the proportions of enhanced, suppressed, or not-modulated neurons depended on retinotopic distance, we counted  
960 the number of each modulation type within 5 deg bins along the retinotopic distance axis, obtaining a  $3 \times 11$  contingency table.  
961 Statistical test for non-uniformity was done using an omnibus chi-square test, which was followed by post-hoc chi-square  
962 tests for each single modulation type.

963 To test whether significantly enhanced neurons were predominantly present close to the injection site, we again applied a  
964 cluster-based permutation approach<sup>S23</sup>. We first calculated the adjusted standardized residuals (ASR) defined as the difference  
965 between the observed counts in the contingency table and the expected counts under the null hypothesis, adjusted for the row  
966 and column totals. For the enhanced neurons, we grouped neighbouring bins with  $|\text{ASR}| \geq 1$  for the enhanced neurons into  
967 clusters, and computed the sum of  $|\text{ASR}|$  in those clusters. We then considered the maximum cluster sum value as the test  
968 statistic. These analysis steps were then repeated over 100000 iterations with randomly permuted distance values across all  
969 neurons. The p-value was the proportion of random permutations which yielded a cluster sum larger than the one from our  
970 original data set.

## 971 Effects of photostimulation on V1 responses

972 For the quantification of effects of optogenetic manipulations on V1 responses, we only considered V1 neurons whose maximal  
973 firing rate exceeded 0.5 sp/s in tuning experiments involving either different directions, sizes, or contrasts. Furthermore, we  
974 excluded neurons, which showed a change in sign of the effect of optogenetic manipulation across experiments. We first  
975 computed, for each unit and experiment, average firing rates during photostimulation in trials with optogenetic manipulation,  
976 and in equivalent time windows in trials of the control condition. We then computed, across experiments, the effect of  
977 photostimulation by taking the difference in average rates between the photostimulation condition and the control condition,  
978 normalized to the rate in the control condition. For the report of average effects of V1 suppression by optogenetic activation of  
979 PV+ inhibitory interneurons, we excluded putative PV+ inhibitory interneurons directly driven by the light, defined as  $\geq 2$ -fold  
980 increase of firing rates in the photostimulation condition compared to the control condition.

## 981 Effects of V1 suppression on dLGN responses

982 To analyze effects of V1 suppression on dLGN responses, we considered neurons located in dLGN (as opposed to e.g. in the  
983 dorsally located hippocampus), if their highest-amplitude extracellular spike waveshape was measured on an electrode channel  
984 including and between channels delineating the top and bottom of dLGN. Top and bottom dLGN channels were defined as the  
985 dorsal most or ventral most channel, respectively, with visually responsive neurons in at least one tuning experiment, involving  
986 gratings of either different directions, sizes, temporal frequencies or contrasts. We defined a neuron being visually responsive in  
987 these tuning experiments if (1) the absolute difference between its mean firing rate to at least 3 conditions within an experiment  
988 and to the interleaved blank condition, was larger than  $2.58 \times$  the standard error of the mean rate in that condition, and (2) if its  
989 maximal firing rate exceeded 0.5 sp/s.

990 For the analysis of effects of V1 photostimulation on dLGN responses to medium gray screen (corresponding to a size  
991 0 deg stimulus, **Figure 2d-g**), we excluded neurons that did never spike in a time window around V1 photostimulation  
992 ( $\pm (0.8 \text{ s} + \Delta t_{\text{opto}})$ ), where  $\Delta t_{\text{opto}}$  is the duration of V1 photostimulation. We focused on experiments with a minimum of

993 5 trials, during which the animal was sitting during the temporal analysis windows of interest. For the assessment of changes in  
994 firing rate, we computed for each unit average firing rate during the window of V1 photostimulation and during a window of  
995 equivalent length immediately preceding light onset. For the analysis of burst ratios, we excluded all neurons that did not spike  
996 either in the control or the photostimulation window, as the ratio of burst spikes to all spikes in such cases is not defined. We  
997 assessed changes in bursting by computing in the same time windows the ratio of burst spikes to the number of all spikes. Burst  
998 spikes were defined according to<sup>117</sup>, and required a silent period of at least 100 ms before the first spike in a burst, followed by  
999 a second spike with an interspike interval < 4 ms. Any subsequent spikes with preceding interspike intervals < 4 ms were also  
1000 considered to be part of the burst. All other spikes were regarded as tonic.

1001 For the analysis of V1 suppression effects on dLGN spatial integration (**Figure 2h-l**), we considered neurons for further  
1002 analysis whose size tuning curves had an  $R^2 \geq 0.7$ . For evaluating the effect of CT feedback on small sizes, we considered, for  
1003 each neuron, the responses at the stimulus size immediately smaller than preferred size; for evaluating the effect on large sizes,  
1004 we considered the responses at the maximal size.

#### 1005 **Comparison of RF sizes in dLGN and visTRN**

1006 To compare classical RF sizes between dLGN and visTRN (**Figure 4d**), we analyzed responses to sparse noise stimuli. We  
1007 focused on units with a mean firing rate of at least 0.15 sp/s, and whose RFs were well-fit ( $R^2 \geq 0.4$ ). If for a given unit, results  
1008 from more than one sparse noise experiment fulfilled these criteria, we selected the experiment in which the RF was best  
1009 captured by the 2D Gaussian (largest  $R^2$  value).

#### 1010 **Spatial integration in visTRN**

1011 To analyze spatial integration in visTRN (**Figure 4e-h** and **Figure 5**), we only considered units whose mean firing rate in the  
1012 control condition was sufficiently high ( $\geq 0.15$  sp/s) and whose size tuning curve in the control condition was well captured  
1013 by the model ( $R^2 \geq 0.7$ ). We further concentrated on experiments in which the stimulus center had been presented inside  
1014 1 sigma of the fitted RF center, focusing on RF fits with  $R^2 \geq 0.4$  obtained from units with sufficiently high mean firing rate  
1015 ( $\geq 0.15$  sp/s). In case a unit fulfilled these criteria for multiple size tuning experiments, we focused on the experiment in which  
1016 responses in the control condition were best captured by the ratio of Gaussians model (largest  $R^2$  value).

1017 Suppression index and preferred size were computed as described above. For few units, our definition of the preferred size  
1018 and the absence of surround suppression led to slightly stronger responses to the largest stimulus as compared to the optimal  
1019 stimulus diameter resulting in negative suppression indices. For these cases, we set the suppression index to 0.

1020 To test if a lack of surround suppression could be explained by the difference between stimulus center and RF center or by  
1021 the difference between monitor center and RF center, we computed Pearson's correlations between the suppression indices and  
1022 the two differences (**Figure S3**). In case multiple valid RF mapping experiments were available for a unit, we used the RF with  
1023 the best model fit (largest  $R^2$  value).

#### 1024 **Quantifying effects of V1 suppression on visTRN responses**

1025 To ensure that suppression indices and preferred size for size tuning curves recorded under V1 suppression can be interpreted,  
1026 we required a minimum mean firing rate of 0.1 sp/s during V1 suppression for the analyses in **Figure 5f-g**. For computing  
1027 population size tuning curves (**Figure 5d**), differences in response rate as a function of stimulus size (**Figure 5h**), and for  
1028 fitting the threshold-linear model (**Figure 5i-j**), we normalized the fitted size tuning curves by dividing them by the maximum  
1029 response across the two conditions.

1030 To analyze differences in response rate between control and photostimulation condition as a function of stimulus size  
1031 (**Figure 5h**), we subtracted for each unit the normalized size tuning curve (1 deg resolution) in the control condition from that  
1032 in the photostimulation condition, and took the mean across the population. To test for a significant change in the effect of  
1033 photostimulation with size, we computed the difference in photostimulation effect for subsequent sizes (1 deg steps) and used a  
1034 resampling procedure across neurons (1000 iterations). If 0 was outside the 97.5<sup>th</sup> percentile of the resulting distribution of  
1035 mean differences, we considered the change significant.

1036 To characterize the change in visTRN size tuning induced by suppression of CT feedback (**Figure 5i-j**), we predicted  
1037 visTRN responses to stimuli of different sizes during V1 suppression based on responses under the control condition by fitting

a threshold-linear model:

$$f(x) = \max(0, m * x + b) \quad (8)$$

1036 If the resulting fit was of good quality ( $R^2 \geq 0.8$ ), we extracted the slope and the threshold parameter (x-intercept).

### 1037 Computational modeling

1038 To explore how dLGN size tuning changes with the spatial scale of the inhibitory CT feedback component we computed response  
1039 curves using `pylgn`<sup>61</sup>, a python toolbox that simulates dLGN responses based on the extended difference-of-Gaussians model<sup>60</sup>  
1040 (**Figure 3**). We evaluated the model in its mixed-feedback configuration where a given dLGN relay cell receives feedback of  
1041 both signs from cortical cells belonging to the On and Off pathway. We took existing code ([https://github.com/miladh/edog-simulations/tree/master/size\\_tuning](https://github.com/miladh/edog-simulations/tree/master/size_tuning)) that had specified the model parameters following insights from the cat visual system  
1042 and adjusted them to mimic more closely the properties of the mouse visual system. For the difference-of-Gaussians which  
1043 represents the receptive field of retinal ganglion cells (RGCs), we approximated width parameters based on data recorded from  
1044 transient OFF- $\alpha$  RGCs<sup>S24</sup>. For the coupling kernels, we scaled the width parameter by a factor of 10, excluding the target  
1045 inhibitory feedback kernel which we varied between 1 and 40 in 1 deg steps. For each inhibitory feedback kernel width we then  
1046 generated tuning curves by simulating responses to static gratings of different size (diameter = 0 - 75; stepsize = 1 deg) with  
1047 and without feedback. Feedback was manipulated by setting the weight of the feedback kernels to either 0 (no-feedback) or 1.  
1048 The resulting curves were normalized so that the maximum response in the no-feedback condition equaled 1. Preferred size and  
1049 suppression index were computed as described for the electrophysiological data.  
1050

1051 **Supplementary Information**

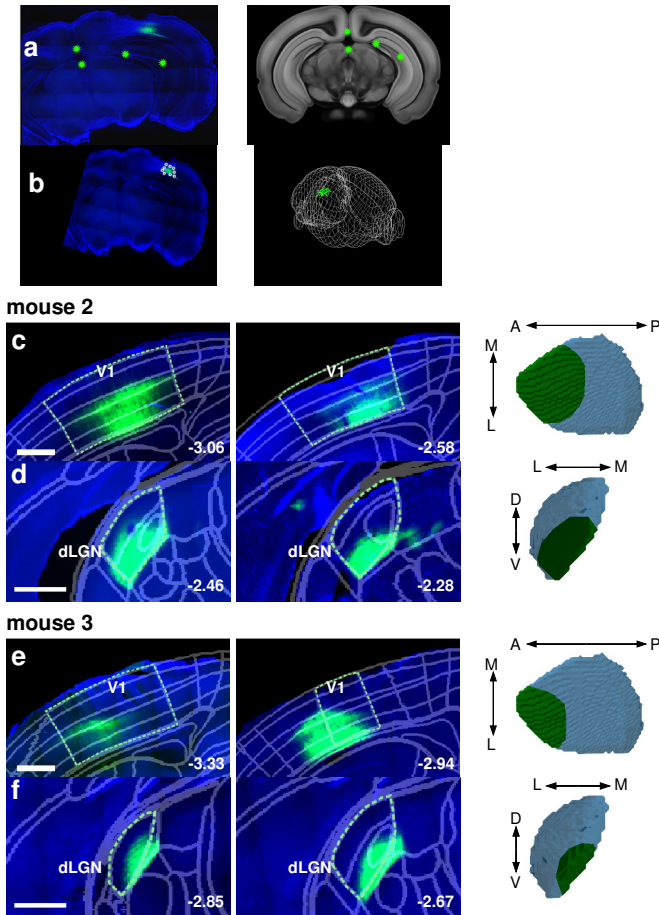


**Figure S1** Pipeline for quantification of expression volumes and expression volumes in the other two mice used for the analysis

(a) *Left*: Manually chosen reference points on salient features of an example brain slice image. *Right*: Corresponding locations of the reference points are marked on the manually chosen atlas section. (b) *Left*: Example brain slice image registered and transformed to the CCF. White points outline the expression zone and are extracted as CCF coordinates. *Right*: All points (green) framing the expression zone in V1 from one animal shown in a 3D boundary mesh of the mouse brain (white). (c) *Left*: Two example sections of mouse 2 containing the expression zone in V1. *Right*: Axial view of 3D reconstruction of the expression volume (green) within V1 L6 (blue). Relative volume = 17%. (d) *Left*: Two example sections of mouse 2 showing the expression zone in dLGN. *Right*: Coronal view of 3D reconstruction of the expression volume (green) within dLGN (blue). Relative volume = 10% (e) Same as (c) for mouse 3. Relative volume = 33% (f) Same as (d) for mouse 3. Relative volume = 21% In (c-f), numbers in bottom right corner indicate distance from Bregma in mm.

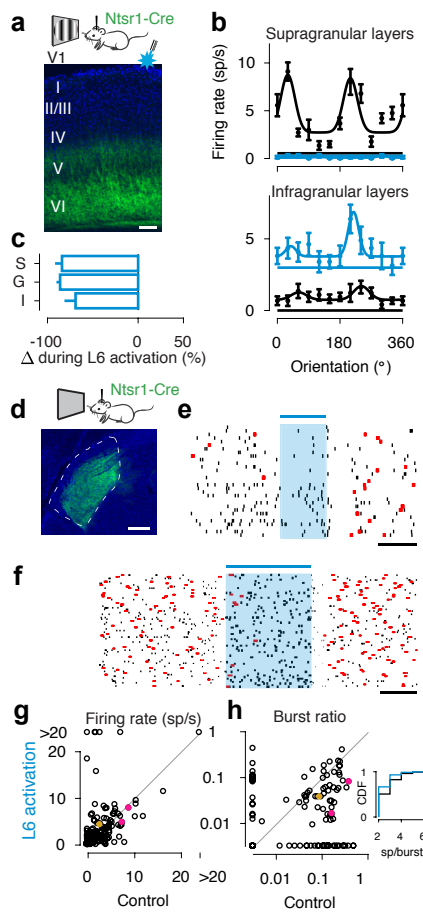


**Figure S2** Photoactivation of L6CT neurons promotes tonic firing mode

(a) Coronal section of V1 of a Ntsr1-Cre mouse injected with cre-dependent AAV-ChR2. *Green*: ChR2-YFP, *blue*: DAPI. Scale bar 100  $\mu$ m. (b) Example orientation tuning curves of cells located in supragranular or infragranular layers for trials during V1 L6CT photoactivation (*blue*) and control conditions (*black*). (c) Percent response change for cells in supragranular (S, n = 72), granular (G, n = 70) and infragranular (I, n = 171) layers, as determined by CSD<sup>58</sup>. More mixed effects in I layers are likely due to a combination of direct activation of L6CT neurons as well as di-synaptic inhibition. All  $p \leq 1.8 \times 10^{-13}$ , Wilcoxon signed-rank test. (d) Coronal slice of dLGN, with L6CT axons expressing ChR2 in *green*. (e-f) Recordings from dLGN. Activity of two example dLGN neurons during spontaneous activity aligned to V1 L6CT photoactivation (*shaded blue*). *Red*: burst spikes, black horizontal bar: 200 ms. (e) n = 31 trials, (f) n = 69 trials. (g) Firing rates during vs. before V1 L6CT photoactivation. n = 167 neurons;  $p = 0.4$ , Wilcoxon signed-rank test. (h) Ratio of burst spikes during vs. before V1 L6CT photoactivation. n = 139 neurons;  $p = 1.7 \times 10^{-7}$ , Wilcoxon signed-rank test). Data points at marginals represent neurons whose burst ratio was 0. *Inset*: cumulative distribution of burst lengths during (*blue*) vs. before (*black*) V1 L6CT photoactivation.

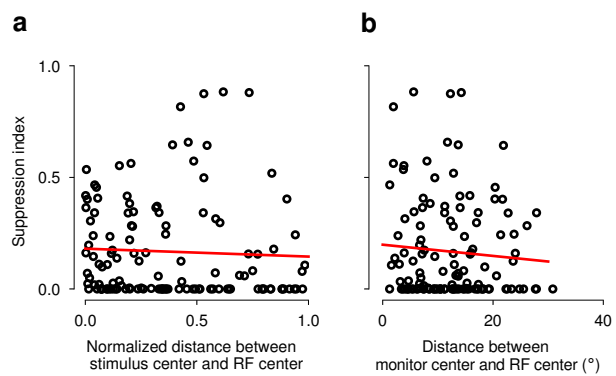


**Figure S3** visTRN suppression indices do not correlate with distance between RF center and monitor or stimulus center.

(a) Suppression indices for visTRN population ( $n = 125$ ) plotted against the normalized distance between stimulus center and their RF center (Red line: fitted linear regression; Pearson's correlation coefficient  $R = -0.05$ ,  $p = 0.60$ ). (b) Suppression indices for visTRN population plotted against the distance between monitor center and their RF center ( $R = -0.08$ ,  $p = 0.39$ ).

<b>integrator settings</b>	
number of spatial points (Nr)	$2^7$
spatial resolution (dr)	1 deg
number of temporal points (Nt)	$2^1$
temporal resolution (dt)	1 ms
<b>stimulus settings</b>	
spatial frequency	0.05 cyc/deg
temporal frequency	0 cyc/ms
patch diameter	start: 0 deg stop: 75 deg count: 76
<b>ganglion difference-of-Gaussians</b>	
center Gaussian	amplitude (A): 1 width (a): 3.33 deg
surround Gaussian	amplitude (B): 0.2 width (b): 7.67 deg
<b>spatial coupling kernels</b>	
excitatory feedforward kernel (Krg)	weight (w): 1 amplitude (A): 1 width (a): 1 deg
inhibitory feedforward kernel (Krig)	weight (w): 0.5 amplitude (A): -1 width (a): 3 deg
excitatory feedback kernel (Krc_ex)	weight (w): 0 / 1 amplitude (A): 0.3 width (a): 1 deg
inhibitory feedback kernel (Krc_in)	weight (w): 0 / 1 amplitude (A): -0.6 width (a): 1 deg - 40 deg, stepsize: 1 deg

**Table S1** eDOG parameters used to simulate dLGN size tuning curves in [Figure 3](#)

## 1052 Supplemental references

1053 [S1] Zolotukhin, S. *et al.* Recombinant adeno-associated virus purification using novel methods improves infectious titer  
1054 and yield. *Gene Ther.* **6**, 973–985 (1999).

1055 [S2] D’Costa, S. *et al.* Practical utilization of recombinant AAV vector reference standards: Focus on vector genomes  
1056 titration by free ITR qPCR. *Mol. Ther. - Methods & Clin. Dev.* **3**, 16019 (2016).

1057 [S3] Grubb, M. S. & Thompson, I. D. Quantitative Characterization of Visual Response Properties in the Mouse Dorsal  
1058 Lateral Geniculate Nucleus. *J. Neurophysiol.* **90**, 3594–3607 (2003).

1059 [S4] Rueden, C. T. *et al.* ImageJ2: ImageJ for the next generation of scientific image data. *BMC Bioinforma.* **18**, 529 (2017).

1060 [S5] Schindelin, J. *et al.* Fiji: An open-source platform for biological-image analysis. *Nat. Methods* **9**, 676–682 (2012).

1061 [S6] Shamash, P., Carandini, M., Harris, K. & Steinmetz, N. A tool for analyzing electrode tracks from slice histology.  
1062 Preprint at <https://www.biorxiv.org/content/10.1101/447995v1> (2018).

1063 [S7] Dombeck, D. A., Khabbaz, A. N., Collman, F., Adelman, T. L. & Tank, D. W. Imaging Large-Scale Neural Activity  
1064 with Cellular Resolution in Awake, Mobile Mice. *Neuron* **56**, 43–57 (2007).

1065 [S8] Pachitariu, M., Steinmetz, N., Kadir, S., Carandini, M. & Harris, K. D. Kilosort: Realtime spike-sorting for extracellular  
1066 electrophysiology with hundreds of channels. Preprint at <https://www.biorxiv.org/content/10.1101/061481v1.abstract>  
1067 (2016).

1068 [S9] Spacek, M. A., Blanche, T. & Swindale, N. Python for large-scale electrophysiology. *Front. Neuroinform.* **2**, 9 (2009).

1069 [S10] Swindale, N. V. & Spacek, M. A. Spike sorting for polytrodes: A divide and conquer approach. *Front. Syst. Neurosci.*  
1070 **8**, 6 (2014).

1071 [S11] Quiroga, R. Q., Nadasdy, Z. & Ben-Shaul, Y. Unsupervised spike detection and sorting with wavelets and superparamagnetic  
1072 clustering. *Neural Comput.* **16**, 1661–1687 (2004).

1073 [S12] Henze, D. A. *et al.* Intracellular Features Predicted by Extracellular Recordings in the Hippocampus In Vivo. *J.  
1074 Neurophysiol.* **84**, 390–400 (2000).

1075 [S13] Hazan, L., Zugaro, M. & Buzsaki, G. Klusters, NeuroScope, NDManager: A free software suite for neurophysiological  
1076 data processing and visualization. *J. Neurosci. Methods* **155**, 207–216 (2006).

1077 [S14] Supèr, H. & Roelfsema, P. R. Chronic multiunit recordings in behaving animals: Advantages and limitations. *Prog.  
1078 Brain Res.* **147**, 263–282 (2005).

1079 [S15] Self, M. W. *et al.* Orientation-tuned surround suppression in mouse visual cortex. *J. Neurosci.* **34**, 9290–304 (2014).

1080 [S16] van der Togt, C., Spekreijse, H. & Supèr, H. Neural responses in cat visual cortex reflect state changes in correlated  
1081 activity. *Eur. J. Neurosci.* **22**, 465–475 (2005).

1082 [S17] Nicholson, C. & Freeman, J. A. Theory of current source-density analysis and determination of conductivity tensor for  
1083 anuran cerebellum. *J. Neurophysio.* **38**, 356–368 (1975).

1084 [S18] Schroeder, C., Mehta, A. & Givre, S. A spatiotemporal profile of visual system activation revealed by current source  
1085 density analysis in the awake macaque. *Cereb. Cortex* **8**, 575–592 (1998).

1086 [S19] Heumann, D., Leuba, G. & Rabinowicz, T. Postnatal development of the mouse cerebral neocortex. II. Quantitative  
1087 cytoarchitectonics of visual and auditory areas. *J. Fur Hirnforschung* **18**, 483–500 (1977).

1088 [S20] Yatsenko, D., Walker, E. Y. & Tolias, A. S. DataJoint: A Simpler Relational Data Model. Preprint at <https://arxiv.org/abs/1807.11104> (2018).

1089 [S21] Liu, B.-h. *et al.* Visual Receptive Field Structure of Cortical Inhibitory Neurons Revealed by Two-Photon Imaging  
1090 Guided Recording. *J. Neurosci.* **29**, 10520–10532 (2009).

1091 [S22] Katzner, S., Busse, L. & Carandini, M. GABA<sub>A</sub> Inhibition Controls Response Gain in Visual Cortex. *J. Neurosci.* **31**,  
1092 5931–5941 (2011).

1094 [S23] Maris, E. & Oostenveld, R. Nonparametric statistical testing of EEG- and MEG-data. *J. Neurosci. Methods* **164**,  
1095 177–190 (2007).

1096 [S24] Ströh, S. *et al.* Eliminating Glutamatergic Input onto Horizontal Cells Changes the Dynamic Range and Receptive  
1097 Field Organization of Mouse Retinal Ganglion Cells. *J. Neurosci.* **38**, 2015–2028 (2018).